Unconventional bulk-Fermi-arc links paired third-order exceptional points splitting from a defective triple point

Jing Hu[1,2,*] Ruo-Yang Zhang[2], Mudi Wang[2], Dongyang Wang[3], Shaojie Ma[4], Jian Huang[1], Linjun Wang[1],
Xiaoping Ouyang[5], Yifei Zhu[6], Hongwei Jia[2,7,†], C. T. Chan[2,‡]

[1]*School of Materials Science and Engineering, Shanghai University, Shanghai, China.*

[2]*Department of Physics, Hong Kong University of Science and Technology, Hong Kong, China.*

[3]*Optoelectronics Research Centre, University of Southampton, Southampton SO17 1BJ, United Kingdom.*

[4]*Department of Optical Science and Engineering, School of Information Science and Technology, Fudan University, Shanghai, China.*

[5]*Northwest Institute of Nuclear Technology, Xi'an, China*

[6]*Department of Mathematics, Southern University of Science and Technology, Shenzhen, China.*

[7]*Institute of Precision Optical Engineering, School of Physics Science and Engineering, Tongji University, Shanghai, China.*

[*] huj@shu.edu.cn ; [†] jiahongwei@tongji.edu.cn ; [‡] phchan@ust.hk

Abstract: Exceptional degeneracies, unique to open systems, are important in non-Hermitian topology. While bulk-Fermi-arcs connecting second-order exceptional points (EP2s) have been observed, the existence of bulk-Fermi-arcs linking higher-order exceptional points remains unexplored. Here, we introduce an unconventional bulk-Fermi-arc in systems with parity-time and pseudo-Hermitian symmetries, which links paired third-order exceptional points (EP3s), where three eigenvalues share identical real parts but distinct imaginary parts. We realize these systems using topological circuits and experimentally demonstrate this unconventional bulk-Fermi-arc. A winding number defined from resultant vector shows that the bulk-Fermi-arc is stabilized by the exchange of Riemannian sheets. Furthermore, analysis via eigenframe deformation and rotation reveals that the EP3 pair is topologically nontrivial and equivalent to a single defective triple point. The EP3s can split from the triple point by varying system parameters, with this splitting protected by topological equivalence. This finding offers insights into non-Hermitian topology with potential applications in wave engineering.

Introduction

The band degeneracies have been extensively recognized as topological defects in parameter space [1-20]. A very typical example of such defects in the three-dimensional (3D) Hermitian setting is the Weyl point [1-7]. Its topological invariant, generally obtained by integrating Berry curvature on a closed surface enclosing the Weyl point, is a crucial measure for predicting Fermi arc surface states at system boundaries [1-6]. Recently, non-Hermitian physics has attracted growing interest as it addresses the ubiquitous open systems that exchange energy with the surrounding environment. The energy exchange is represented by the imaginary parts of the complex eigenvalues, which significantly expands the classes of topological phases of matter [10-23]. The exceptional point (EP) is a unique feature of non-Hermiticity, featuring the coalescence of both eigenvalues and eigenstates. In two dimensional (2D) systems, a pair of EPs of order two (EP2) can be obtained by splitting a topologically nontrivial Dirac point by introducing non-Hermitian perturbations. Due to the eigenvalue braiding around each EP, the EPs generally carry half-quantized topological invariants, known as energy vorticity, resulting in a stable bulk-Fermi-arc (BFA) linking the pair of EP2s [11-13]. This is fundamentally distinct from the commonly observed Fermi-arc surface states that arise from the 2D projection of Weyl points in 3D Hermitian systems [1,3-6], while the BFA resides in the bulk dispersion of a 2D system supporting the EP pairs [11-13]. So far, the BFA is widely recognized as a stable link of EP2s. However, other forms of BFAs, which link higher-order EPs, remain unexplored.

In this study, we unveil an unconventional BFA linking paired exceptional points of order three (EP3), which can widely exist in 2D non-Hermitian systems with parity-time (*PT*) symmetry and an additional pseudo-Hermitian symmetry. High-order exceptional points, unlike second-order ones, are multifold degeneracies where three or more eigenvalues and their eigenstates coalesce [21-24]. These points, common in non-Hermitian systems, enable unique applications such as enhanced sensitivity and the realization of exotic topological structures, making them useful for advancing sensing technologies and exploring novel physical phenomena [25,26]. In 2D systems with multiple eigenstates, the EP3s can exist in the form of cusps that are located entirely on exceptional lines (EL) under the protection of *PT* symmetry [20-22,27]. Here we reveal that by imposing an additional pseudo-Hermitian symmetry, EP3s can emerge in pairs. Unexpectedly, these paired EP3s are stably connected by an unconventional form of BFA, on which the three eigenvalues possess identical real parts but disparate imaginary parts, significantly distinguished from the conventional form. By defining winding numbers using a resultant vector [22], we find that the paired EP3s possess opposite winding numbers, indicating inverse exchanging processes of Riemannian sheets around the two EP3s, which stabilizes the unconventional BFA. The two EP3s linked by the BFA originate from the splitting of an accidental three-fold degeneracy that holds two linearly independent eigenstates (dubbed a defective triple point, DTP), which is also distinguished from the conventional case. It is known that paired EP2s stably linked by a BFA carry nontrivial eigenvector topology [11,12]. However, prior topological characterization for high-order EPs that utilizes the resultants, which primarily focuses on the eigenvalues [21,22], cannot reveal the topological nontriviality of eigenvectors of the EP3 pair. To address this limitation, we incorporate the eigenvectors and employ the notion of eigenframe deformation and rotation, which aligns with the intersection homotopy [28,29], to characterize the topology of such singularities that are located entirely on ELs. The paired EP3s, which possess opposite winding numbers of resultant vectors and are connected by the BFA, are shown to have a nontrivial topology identical to that of the DTP. Therefore, the splitting of the

EP3s from the DTP is topologically protected. Finally, by realizing such systems with nonreciprocal circuits, the new form of BFA is experimentally demonstrated.

Results and Discussion

We start with a direct comparison between the two forms of BFAs. As shown in Fig. 1a, a 2D Hermitian system with *PT* symmetry generally displays Dirac point degeneracies as linear crossings of two bands. By introducing non-Hermitian perturbations with specific symmetries, the Dirac point is split into a pair of EP2s (see Fig. 1b), which are stably connected by the conventional BFA with two eigenvalues sharing identical real parts but different imaginary parts [11-13]. The unconventional BFA we study is inherently different. We consider the following 2D non-Hermitian Hamiltonian with three eigenstates,

$$H=\begin{bmatrix} -g(f_x,f_y)-f_x+1 & -g(f_x,f_y) & -f_x \\ g(f_x,f_y) & g(f_x,f_y)+f_y & -f_y \\ f_x & -f_y & f_x+f_y \end{bmatrix} \tag{1}$$

where f_x and f_y are real and constitute the 2D parameter space. This non-Hermitian Hamiltonian is chosen to manifest both *PT* symmetry and an additional η-pseudo-Hermitian symmetry [30,31] ($\eta H\eta^{-1}=H^{\dagger}$, η takes the form of Minkowski metric η=diag(-1,1,1) [32]). The specific function $g(f_x, f_y)$ =0.343-f_x +b is chosen because it exhibits an accidental three-fold degeneracy at b=0, as shown in Fig. 1c. This degeneracy is defective and has two linearly independent eigenstates, which we therefore refer to as a defective triple point (DTP). By introducing perturbations while preserving the symmetries (simply by tuning b), this DTP can split into a pair of EP3s lying on the cusps of ELs. The EP3s are stably connected by a special type of BFA, which resides in the broken phase region, as displayed in Fig. 1d. We note that the three eigenvalues on the BFA have identical real parts, while their imaginary parts are different. The DTP should be distinguished from the EP3, despite that they are both defective three-fold degeneracies, due to the fact that the EP3 only has one eigenstate.

To experimentally observe the unconventional BFA, we employ a nonreciprocal electric circuit that incorporates three nodes (labeled **A**, **B**, and **C** in Fig. 2a) to emulate the hoppings in a three-state non-Hermitian model. The tight-binding hopping parameters are utilized to construct a synthetic 2D parameter space. The electric circuit platform [33-37] offers significant advantages over others in implementing and precisely controlling complex nonreciprocal hoppings, thanks to the diverse range of readily available active circuit elements. Nonreciprocity in electric circuits refers to the direction-dependent transfer of signals or energy between two nodes, enabling functionalities such as directional amplification and robust unidirectional transport. This is often achieved using a negative impedance converter with current inversion (INIC), an active circuit element that breaks reciprocity by introducing asymmetric hopping parameters [34,37]. The *PT* symmetry inherent to the non-Hermitian system ensures that these asymmetric hopping parameters are real and can be implemented using conductance or inductance combined with the INIC[35]. The structure of the circuit elements and their corresponding hopping parameters are shown in the left panel of Fig. 2a . Specifically, an INIC in series with a capacitor, denoted as $\pm C_i$ (see right panel of Fig. 2a), is employed to achieve the nonreciprocal hoppings depicted. In this setup, the circuit's admittance matrix J and its eigenvalues, labeled j, are analogous to the Hamiltonian matrix and energy spectra, respectively [33,34,36]. In the experiment, we applied current inputs to each of the three nodes and measured the resulting voltage responses. From these measurements, we constructed the matrix-form Green's function, whose inverse yields the circuit Laplacian, enabling the analysis of its eigenvalue and eigenstate spectra. Further details on the experimental implementation and measurements can be found in Methods.

We first observe the unperturbed case (b=0) where the DTP is present on the 2D plane of dispersion diagram. From left panel of Fig. 2b, we see that four ELs (orange lines) emerge from the DTP (red star), three with $f_y > 0.121$ and one with $f_y < 0.121$, and we measured the admittance bands marked by the three dashed lines (f_y=0.3, 0.121 and 0.01), which are shown in the right panel of Fig. 2b. It can be identified that three of the ELs are formed by the degeneracies of the 2nd and the 3rd bands (f_y=0.3 and 0.01, right panel), while the other is formed by the 1st and the 2nd bands (f_y=0.3, right panel). The DTP therefore serves as the aggregation node of all the ELs. By introducing the perturbations (b=0.0299), the DTP is split into two EP3s lying on the cusps of ELs (see the left panel of Fig. 2c). We see that each of the EP3s are connected by two ELs, and one EL is formed by the degeneracy of the 1st and the 2nd bands, while the other is formed by the degeneracy of the 2nd and the 3rd bands (see the right panel of Fig. 2c). The unconventional BFA (blue line in Fig. 2c), on which the real parts of all three eigenvalues coalesce, can be clearly indicated by the experimental results in the right panel of Fig. 2c. By further increasing the perturbations (b=0.0569), the separation between the paired EP3s in parameter space becomes larger. However, the BFA is stable against this perturbation, which still stably links the two EP3s, as shown in the left panel of Fig. 2d. Additionally, from the right panel of Fig. 2d, we observe that the dispersive nature on the BFA that the real parts of all three eigenvalues coalesce remains intact regardless of increasing the perturbation in the Hamiltonian. This experimental result demonstrates the stability of the BFA, which comes from the topological nontriviality of the paired EP3s.

Now we delve into the topological aspects of the stability of the unconventional BFA. As we have claimed, the assembling of the paired EP3s is topologically nontrivial. This point of view compliments the conventional understanding where the winding number of cusps of ELs are defined with the resultant vector [21,22],

$$W = \frac{1}{2\pi} \sum_{\alpha=x,y} \oint_{l_\lambda} \frac{(R_1 \partial R_2 / \partial f_\alpha - R_2 \partial R_1 / \partial f_\alpha) df_\alpha}{|R_2^2 + R_1^2|} \tag{2}$$

and the integration results for the two EP3s are W=±1. Here l_λ denotes a closed loop enclosing a single EP3, e.g., L_1 or L_2, as displayed in the lower panel of Fig. 3a. R_1 and R_2 denote the components of the resultant vector field. Details on obtaining the resultant vector and deriving Eq. (2) are shown in Supplementary Note 2. The opposite windings arise from the fact that the eigenvalues undergo converse exchanges of Riemannian sheets around the two EP3s. As can be observed in Fig. 3b and 3c (theoretical: solid lines, experimental: symbols), along loops L_1 and L_2, the eigenvalues j_2 and j_3 are initially coincident because the starting point (SP) of loop L_1 is selected to be on the EL formed by j_2 and j_3 (see stars in the lower panel of Fig. 3a). As the tracking point on L_1 departs from the EL, the degeneracy point of j_2 and j_3 bifurcates. j_2 will then coalesce with j_1 as the tracking point approaches the other EL along L_1. From this point, j_1 and j_2 form a common Riemannian sheet in their real part dispersions because they become conjugated. Finally, when the eigenvalues continue to evolve with the moving of the tracking point along L_1, the three eigenvalues exchange their order $j_1j_2 \leftrightarrow j_3$ (indicated by the vertical dashed lines), which indicates the exchange of two Riemannian sheets - one shared by Re(j_1) and Re(j_2), and the other by j_3. The eigenvalues on loop L_2 simply experience the reverted order exchange process. As shown in Fig. 3c, j_1 and j_2, initially coalesce at SP, bifurcate as the tracking point departs from the EL. Next, j_2 coalesces, bifurcates, and finally coalesces again with j_3, through which they swap with j_1 ($j_1 \leftrightarrow j_2j_3$, indicated by the dashed lines). The BFA is stable because it arises from the intersection of the two Riemannian sheets, an inevitable consequence when these sheets exchange orders (indicated by the nonzero winding W) as they evolve around the EP3s.

We expect that the assembling of paired EPs linked by the BFA should carry nontrivial topology [11,12]. However, applying Eq. (2) on a closed loop encircling both EP3s (on loop L_3) yields a trivial result (W=0) because the order exchange of eigenvalues cancels out on L_3. This is clearly indicated by the vertical dashed lines in Fig. 3d, showing the evolution of eigenvalues along the loop. Therefore, considering only the eigenvalues is insufficient to demonstrate the topological nontriviality of the paired EP3s. In topological band theories, additional topological characteristics are encoded in the evolution of eigenstates, such as the

Berry phase [35] and the homotopical invariants [8]. However, such approaches may not be applicable here due to the presence of ELs on the loops. We therefore employ an intuitively meaningful approach that utilizes the notion of intersection homotopy [20,21,28,29] to characterize the topology of such non-isolated singularities. The symmetry of system (*PT* and pseudo-Hermitian) reveals that the eigenstates obey the Minkowski-type orthogonal relation

$$\varphi_i^T \eta \varphi_j \begin{cases} = 0 & i \neq j \\ \neq 0 & i = j \end{cases} \tag{3}$$

which further determines that the eigenframe evolves in the form of deformation and rotation when the Hamiltonian changes in parameter space. Here we employ the eigenframe approach to implement topological characterization because the eigenframe deformation allows the eigenstates to be parallel within the evolution process, and thus intersecting ELs by the loop (i.e. L_3 in Fig. 3a) is allowed. Additionally, the topological characterization result with eigenframe does not depend on how the conjugate eigenstates are ordered in broken phase sectors (see details in Supplementary Note 3.3). This approach therefore effectively addresses the gap closing on the ELs where the loops intersect [20]. The evolution process along L_3 is provided in Fig. 3e and 3f, corresponding to the real and imaginary parts of eigenstates, respectively. The eigenframe deformation process is obvious because the right eigenstates are not always orthogonal to each other, and sometimes they become parallel or antiparallel when the tracking point approaches ELs, resulting from the Minkowski-type orthogonal relationship (see Supplementary Fig. S6). After a cycle of evolution along L_3, the eigenstates φ_1 and φ_3 evolve to their antipodal points (indicated by the red and black dashed lines) but φ_2 evolves to the initial state without changing the sign ($\varphi_1 \to -\varphi_1, \varphi_2 \to \varphi_2$ and $\varphi_3 \to -\varphi_3$), which is protected by the *PT* symmetry. This indicates that both φ_1 and φ_3 experience quantized accumulated angle π (see the lower panel of Fig. 3e) to their initial states $\theta = \arccos(\varphi^T \cdot \varphi_i)$ (here φ_i denotes the initial state). The imaginary parts of eigenstates serve as an intermediate process because the initial and final states (and the accumulated angle) are real (see Fig. 3f). Notably, the accumulated angles of the eigenstates are not quantized along L_1 and L_2, because eigenstates exchange orders within the evolution process (see Fig. 3b and 3c). By tuning the system parameters, the two EP3s can merge into a DTP, with the eigenframe evolution on a closed loop encircling the DTP being identical to that in Fig. 3e and 3f (results provided in Supplementary Fig. S7 to avoid redundancy). This demonstrates that the EP3 pair is topological equivalent to the DTP from an eigenframe rotation/deformation perspective. Therefore, the merging of the paired EP3s into a single DTP is a consequence of topological conservation. Additionally, due to this topological nontriviality, the DTP cannot be totally eliminated, but will be split into an intersection of ELs and an isolated Dirac point by varying b from 0 to negative.

Conclusion

In summary, we unveil an unconventional BFA that stably connects paired EP3s located at the cusps of ELs in non-Hermitian systems with *PT* symmetry and an additional pseudo-Hermitian symmetry. The winding numbers of the EP3s can be defined with the resultant vectors, and the assembling of EP3s carrying opposite windings of resultant vectors is topologically nontrivial and can coalesce into a DTP under symmetry-preserving parameter changes. This perspective complements the conventional topological understandings of cusps ELs based on resultant vectors [21,22]. The topological nontriviality of the EP3 pair (or the DPT) is characterized through the eigenframe deformation and rotation process. Our topological characterization transcends the traditional theories that only consider the evolution of eigenvalues, offering a more holistic theoretical understanding for a generic non-Hermitian singularities. Moreover, by implementing the system in a nonreciprocal circuit, we experimentally demonstrate the BFA. The study extends the notion of BFA from EP2s to higher order EP3s. It is thus a direct motivation for exploring other forms of BFA linking even higher order EP pairs (e.g., EP4s) that are protected by symmetries in parameter space. Future work may focus on realizing the BFA in periodic systems, offering platforms to explore the finite-size effects associated with it. Our discovery also opens new avenues for wave manipulation and precise control in non-Hermitian systems. The topological robustness of these bulk-Fermi-arcs serves as a basis for designing advanced devices tailored for energy transport, high-sensitivity sensing, and sophisticated signal processing. These results lay a solid foundation for innovative applications in wave engineering and next-generation photonic technologies.

Methods

In our circuit design, a Negative Impedance Converter through Current Inversion (INIC) is implemented, using two equal resisters R_a in both the positive and negative feedback paths (Fig. 2b), enabling precise emulation of nonreciprocal hoppings. The output current I_{out} is opposite to the input current I_{in}, making the capacitance behave as C_i when observed from the output node, while as $-C_i$ when observed from the input node. The designed circuit sample includes three nodes (labeled **A**, **B** and **C** in Fig. 2a) that simulate the nonreciprocal hoppings in the three-state non-Hermitian model [Eq. (1)]. The circuit obeys Kirchhoff's law, expressed as $I = JV$, where I is the input current vector, V represents the node voltages, and J is the admittance matrix. In the grounded configuration, the system is described by:

$$J = D + W - C, \tag{4}$$

where D is the conductance matrix, W is the ground matrix, and C is the adjacency matrix. For our circuit sample in Fig. 2a, the three matrixes can be respectively expressed as:

$$D = \mathrm{diag}(-i\omega C_1 - i\omega C_x, i\omega C_1 + i\omega C_y, i\omega C_x + i\omega C_y), \tag{5}$$

$$W = \mathrm{diag}(i\omega C_{ga} + 1/R_{ga}, i\omega C_{gb} + 1/R_{gb}, i\omega C_{gc} + 1/R_{gc}), \tag{6}$$

$$C = i\omega \begin{bmatrix} 0 & C_1 & C_x \\ -C_1 & 0 & C_y \\ -C_x & C_y & 0 \end{bmatrix}. \tag{7}$$

In our design, we set the grounded capacitance and resistance respectively as

$$C_{gb} = C_{gc} = C_0, C_{ga} = C_0 + c, R_{ga} = R_{gb} = R_{gc} = R_0, \tag{8}$$

and the hopping capacitance as:

$$C_1 = g(f_x, f_y)c,\ C_x = f_x c, C_y = f_y c, \tag{9}$$

where C_0=1nF, R_0=1MΩ and c=10nF. By inserting Eqs. (5-9) into Eq. (4), The admittance matrix yields:

$$J = (i\omega C_0 + 1/R_0) + i\omega c \underbrace{\begin{bmatrix} -g(f_x, f_y) - f_x + 1 & -g(f_x, f_y) & -f_x \\ g(f_x, f_y) & g(f_x, f_y) + f_y & -f_y \\ f_x & -f_y & f_x + f_y \end{bmatrix}}_{H}. \tag{10}$$

Here, we can confirm that the second term realizes the three-state non-Hermitian matrix H in Eq.(1). Since the driving frequency is an external parameter (1kHz in experiments), $\omega=2\pi f$ is also constant. The first term is also unchanged, causing only a complex shift in the eigenvalues without affecting the eigenstates. As a result, the parameters can be precisely adjusted by modifying the corresponding capacitances in Eq.(9) as needed.

The experimental setup, including the circuit samples, is shown in Supplementary Fig. S1. we use surface-mounted device (SMD) capacitors, resistors, and operational amplifiers (OpAmps, model ADA4625-1ARDZ-R7) on a printed circuit board (PCB). Capacitors are connected in parallel between adjacent nodes, with toggle switches allowing flexible selection of capacitance values.

In experimental operation, the OpAmps are powered by two DC power supply (RS PRO Bench Power Supply, 0 →30V, 0→5A) with dual voltages of +5V and –5V. A waveform generator (Keysight: M3201A) drives sinusoidal voltage (1V - 2V at 1kHz) applied to each node, with the voltage response measured via an oscilloscope (RS PRO IDS1074B). Input current is determined by a shunt resistor (4.21 kΩ) connected from the input node to the voltage source. Analyzing the voltage response to the input current yields the admittance matrix J, which contributes to the admittance eigenvalues and eigenstates, facilitating observation of the bulk-Fermi-arc.

Acknowledgements: This work is supported by National Key R&D Program of China (No. 2023YFA1608703) and Hong Kong RGC grants (No. AoE/P-502/20 and 16307821).

Author contributions: H.Jia. and C.T.Chan. planned the project. J.Hu. and H.Jia. designed the sample. J.Hu. carried out the measurements with the help of M.Wang. and D.Wang.. J.Hu. and H.Jia. analyzed the data. R.Y.Zhang. and H.Jia. constructed the theoretical framework. J.Hu., H.Jia. and C.T.Chan. wrote the manuscript. J.Hu., R.Y.Zhang., S.Ma., J.Huang., L.Wang., X.Ouyang., Y.Zhu., H.Jia. and C.T.Chan. contributed to the discussion.

Competing interests: All authors declare no competing interesting.

Additional Information:

Supplementary Information is available for this paper.

Correspondence and requests for materials should be addressed to: huj@shu.edu.cn; jiahongwei@tongji.edu.cn; phchan@ust.hk

Data availability: All data are available in the main text and the supplementary information.

Code availability: The code is available from the corresponding author on reasonable request.

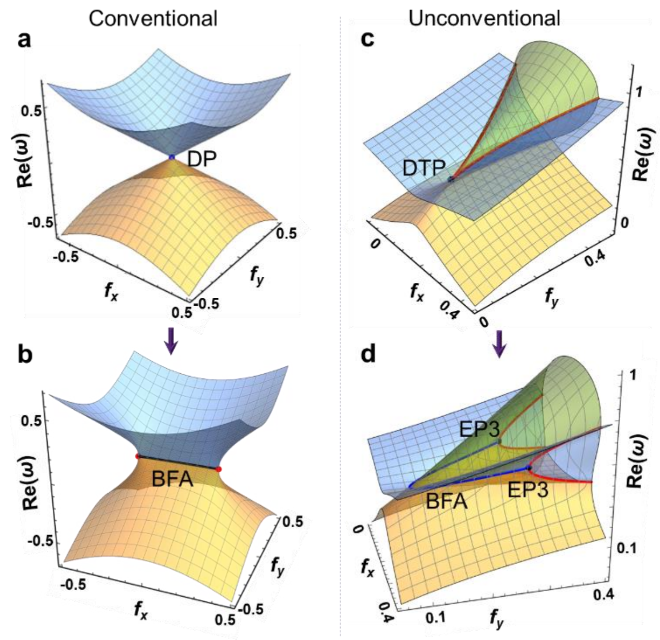

Fig. 1| Comparison between the conventional BFA and the unconventional BFA. **a**, Dispersion diagram near the 2D Dirac point (DP), obtained with the *PT* symmetric Hermitian Hamiltonian $H = f_x\sigma_1 + f_y\sigma_3$. Re($\omega$) denotes real part of eigenvalues as a function of f_x and f_y for the two eigenvalues in orange and blue, respectively. **b**, Paired second order exceptional points (EP2, red dots) obtained from splitting the DP by introducing gain and loss term $qi\sigma_3$ to the Dirac Hamiltonian ($\sigma_{1\sim3}$ denote Pauli matrices), where q is the perturbation term. The paired EP2s are stably connected by the conventional bulk-Fermi-arc (BFA). The eigenvalues on the conventional BFA are conjugate to each other (real parts coalescence). **c**, Dispersion diagram near the defective triple point (DTP) on the 2D parameter space. The red lines denote ELs, and the DTP is embedded on the ELs. The three real eigenvalues are marked in orange, blue and green, respectively. **d**, Paired EP3s obtained from splitting the DTP by introducing perturbations with symmetries preserved. EP3s are both cusps of ELs, which are stably connected by the unconventional BFA residing in the broken phase domain. The three eigenvalues on the unconventional BFA share identical real parts and have different imaginary parts. Two of the three eigenvalues on the unconventional BFA are conjugate to each other, while the other eigenvalue is real.

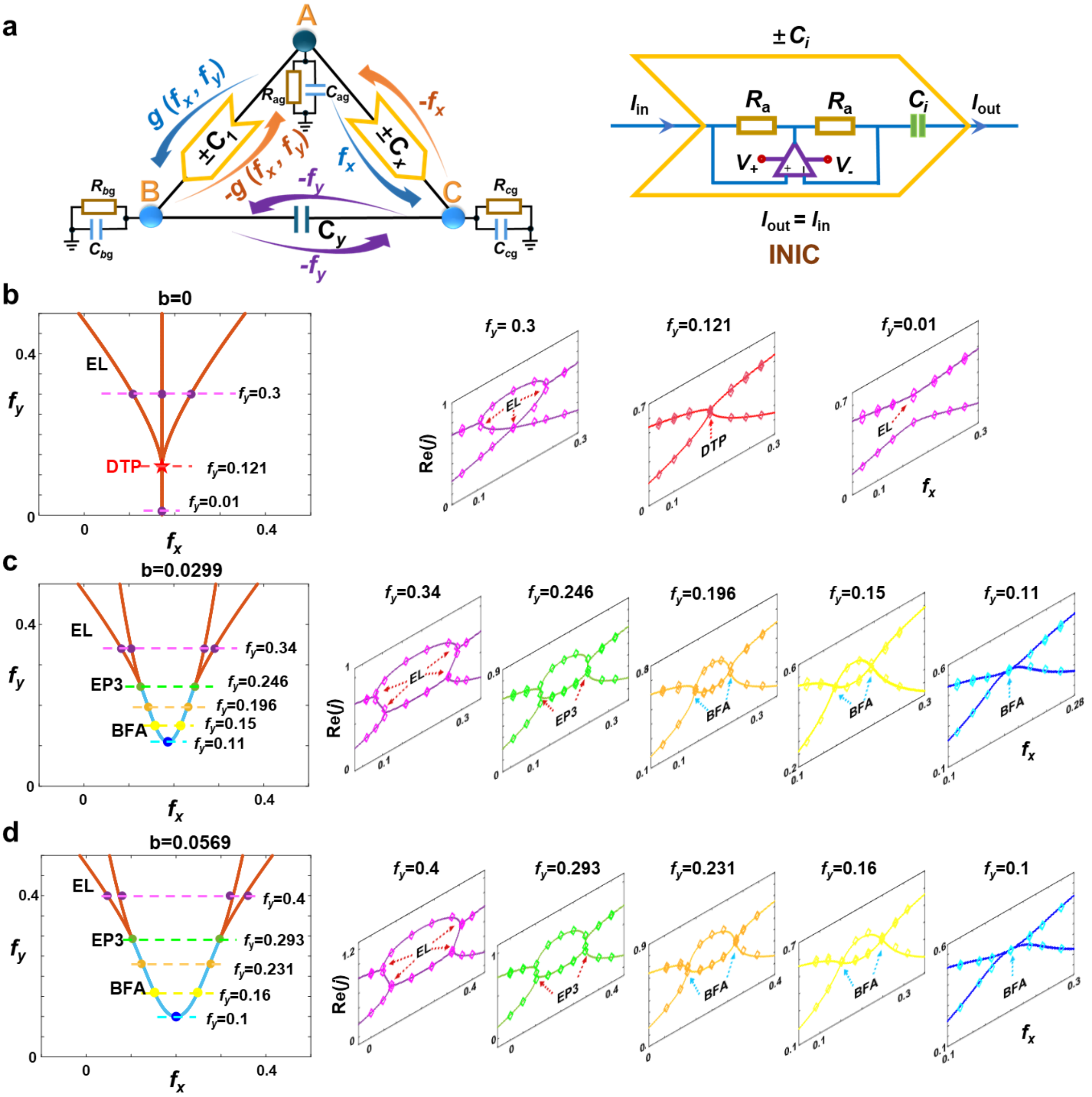

Fig. 2| Experimental observation of the unconventional BFA with topological circuit. **a**, implementation of the Hamiltonian. Left panel: The system includes three nodes **A**, **B** and **C**. The hoppings between **A** and **B**, and between **A** and **C** are nonreciprocal hoppings, implemented using an impedance converter with current inversion (INIC) circuit in series with capacitors (C_1, C_x). The hopping between **B** and **C** is reciprocal, realized with a pure capacitor (C_y). The hoppings between **A** and **C** and between **B** and **C** implement synthetic dimensions f_x and f_y, and the hopping between **A** and **B** is a linear function of f_x and f_y, $g(f_x,f_y)=0.343-f_x+b$. Here, b in the linear function denotes the perturbation term. R_{ag}, R_{bg} and R_{cg} are all grounded resistors; C_{ag}, C_{bg} and C_{cg} are all grounded capacitors. Right panel: INIC structure, with two equal resisters R_a in both the positive and negative feedback paths, and capacitor C_i in series. **b-d,** Experimental measurements of admittance eigenvalues for the cut planes with perturbation term b=0 (**b**), b=0.0299 (**c**) and b=0.0569 (**d**), respectively. Left panels: Degeneracies in the synthetic 2D parameter space on these cut planes. The ELs, DTP and BFAs are denoted by the orange lines, red star, and blue line, respectively. The experimentally identified degeneracies are marked with solid dots. Dashed lines in different color correspond to the measured lines (f_y =t) on the right panels. Right panels: Real parts of the dispersion of eigenvalues as a function of f_x for different f_y lines (f_y =t) on the corresponding cut planes. The eigenvalues are ordered in exact phases from small to large. The experimentally measured admittance eigenvalues are marked in circles, and all the degeneracies (EL, DTP, EP3 and BFA) are indicated by arrows. The experimental error bars are provided in Supplementary Note 1. The unconventional BFA can be found to stably connect the paired EP3s. Increasing the perturbation simply enlarges the interspace between the two EP3s, but cannot eliminate the BFA, demonstrating the stability of the BFA. Experimental raw data for plotting (**b**-**d**) is provided in the Supplementary Data.

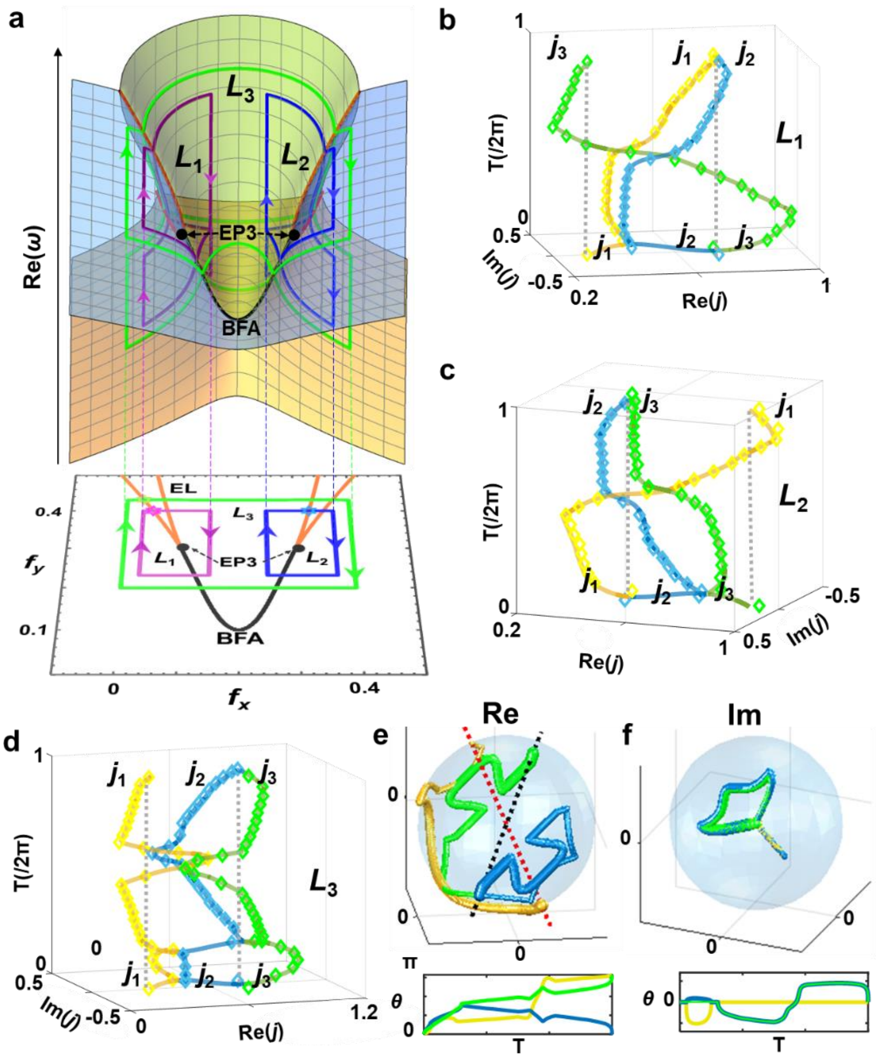

Fig. 3| Topological understanding of the unconventional BFA and the paired EP3s. **a**. Two closed loops encircling each of the paired EP3s (purple loop L_1, and blue loop L_2), and another loop encircling both (green loop L_3). The eigenvalues on the loops are shown in the upper panel, and the structures of the loops in the 2D parameter space are shown in the lower panel. **b** and **c**. The eigenvalue evolution processes along L_1(**b**) and L_2 (**c**), respectively. The eigenvalues j_1 and j_2 and j_3 are colored in yellow, blue and green, respectively. The order exchange processes are inverse along L_1 and L_2. For L_1, j_1 and j_2 coalesce and swap with j_3 ($j_{1,2} \leftrightarrow j_3$), while for L_2, j_2 and j_3 coalesce and swap with j_1 ($j_1 \leftrightarrow j_{2,3}$). **d.** The eigenvalue evolution processes along L_3. The eigenvalues do not experience order exchange along L_3. The solid lines and rhombus symbols in panels b, c and d correspond to theoretical and experimental results, respectively. **e** and **f.** Demonstration of the nontrivial topology of the paired EP3s with the evolution process of eigenframe along L_3, corresponding to the real and imaginary parts of eigenstates, respectively. The eigenstates φ_1 and φ_2 and φ_3 are also colored in yellow, blue and green, respectively. The lower panels show the corresponding accumulated angles to the initial states. We see that the imaginary parts of eigenstates serve as intermediate process. Eigenstates φ_1 and φ_3 accumulate nontrivial quantized angle π, and thus their final states are on the antipodal points to the initial states. The accumulated angle for φ_2 is zero. The experimental raw data for plotting the symbols in (**b**-**d**) is provided in the Supplementary Data.

References:

1. Wan, X., Turner, A. M., Vishwanath, A., et al. Topological semimetal and Fermi-arc surface states in the electronic structure of pyrochlore iridates. *Phys. Rev. B* **83,** 205101 (2011).
2. Lu, L., Wang, Z., Ye, D., et al. Experimental observation of Weyl points. *Science* **349,** 622–624 (2015).
3. Noh, J., Huang, S., Leykam, D., et al. Experimental observation of optical Weyl points and Fermi arc-like surface states. *Nat. Phys.* **13,** 611–617 (2017).
4. He, H., Qiu, C., Cai, X., et al. Observation of quadratic Weyl points and double-helicoid arcs. *Nat. Commun.* **11,** 1820 (2020).
5. Wang, Q., Xiao, M., Liu, H., et al. Optical interface states protected by synthetic Weyl points. *Phys. Rev. X* **7,** 031032 (2017).
6. Yang, B., Guo, Q., Tremain, B., et al. Ideal Weyl points and helicoid surface states in artificial photonic crystal structures. *Science* **359,** 1013–1016 (2018).
7. Lu, L., Fu, L., Joannopoulos, J. D., et al. Weyl points and line nodes in gyroid photonic crystals. *Nat. Photon.* **7,** 294–299 (2013).
8. Wu, Q. S., Soluyanov, A. A. & Bzdušek, T. Non-Abelian band topology in noninteracting metals. *Science* **365,** 1273–1277 (2019).
9. Bzdušek, T., Wu, Q. S., Rüegg, A., et al. Nodal-chain metals. *Nature* **538,** 75–78 (2016).
10. Miri, M. A. & Alù, A. Exceptional points in optics and photonics. *Science* **363,** eaar7709 (2019).
11. Kawabata, K., Bessho, T. & Sato, M. Classification of exceptional points and non-Hermitian topological semimetals. *Phys. Rev. Lett.* **123,** 066405 (2019).
12. Zhou, H., Peng, C., Yoon, Y., et al. Observation of bulk Fermi arc and polarization half charge from paired exceptional points. *Science* **359,** 1009–1012 (2018).
13. Kozii, V. & Fu, L. Non-Hermitian topological theory of finite-lifetime quasiparticles: Prediction of bulk Fermi arc due to exceptional point. *Phys. Rev. B* **109,** 235139 (2024).
14. Wang, C., Sweeney, W. R., Stone, A. D., et al. Coherent perfect absorption at an exceptional point. *Science* **373,** 1261–1265 (2021).
15. Ding, K., Fang, C. & Ma, G. Non-Hermitian topology and exceptional-point geometries. *Nat. Rev. Phys.* **4,** 745–760 (2022).

16. Doppler, J., Mailybaev, A. A., Böhm, J., et al. Dynamically encircling an exceptional point for asymmetric mode switching. *Nature* **537,** 76–79 (2016).

17. Özdemir, Ş. K., Rotter, S., Nori, F., et al. Parity–time symmetry and exceptional points in photonics. *Nat. Mater.* **18,** 783–798 (2019).

18. Hodaei, H., Hassan, A. U., Wittek, S., et al. Enhanced sensitivity at higher-order exceptional points. *Nature* **548,** 187–191 (2017).

19. Jia, H., Zhang, R. Y., Hu, J., et al. Topological classification for intersection singularities of exceptional surfaces in pseudo-Hermitian systems. *Commun. Phys.* **6,** 293 (2023).

20. Hu, J., Zhang, R. Y., Wang, Y., et al. Non-Hermitian swallowtail catastrophe revealing transitions among diverse topological singularities. *Nat. Phys.* **19,** 1098–1103 (2023).

21. Tang, W., Ding, K. & Ma, G. Realization and topological properties of third-order exceptional lines embedded in exceptional surfaces. *Nat. Commun.* **14,** 6660 (2023).

22. Delplace, P., Yoshida, T. & Hatsugai, Y. Symmetry-protected multifold exceptional points and their topological characterization. *Phys. Rev. Lett.* **127,** 186602 (2021).

23. Mandal, I. & Bergholtz, E. J. Symmetry and higher-order exceptional points. *Phys. Rev. Lett.* **127**, 186601 (2021).

24. Montag, A. & Kunst, F. K. Symmetry-induced higher-order exceptional points in two dimensions. *Phys. Rev. Res.* **6**, 023205 (2024).

25. Hodaei, H., Hassan, A. U., Wittek, S. et al. Enhanced sensitivity at higher-order exceptional points. *Nature* **548**, 187–191 (2017).

26. Wang, K., Xiao, L., Lin, H. et al. Experimental simulation of symmetry-protected higher-order exceptional points with single photons. *Sci. Adv.* **9**, eadi0732 (2023).

27. Mandal, I. & Bergholtz, E. J. Symmetry and higher-order exceptional points. *Phys. Rev. Lett.* **127,** 186601 (2021).

28. Kirwan, F. & Woolf, J. *An introduction to intersection homology theory* (CRC Press, 2006).

29. Gajer, P. *The intersection Dold-Thom theorem* (State University of New York at Stony Brook, 1993).

30. Mostafazadeh, A. Pseudo-Hermitian representation of quantum mechanics. *Int. J. Geom. Methods M.* **7,** 1191–1306 (2010).

31. Mostafazadeh, A. & Batal, A. Physical aspects of pseudo-Hermitian and PT-symmetric quantum mechanics. *J. Phys. A* **37,** 11645 (2004).

32. Freedman, D. Z. & Van Proeyen, A. *Supergravity* (Cambridge University Press, 2012).

33. Imhof, S., Berger, C., Bayer, F., et al. Topolectrical-circuit realization of topological corner modes. *Nat. Phys.* **14,** 925–929 (2018).

34. Helbig, T., Hofmann, T., Imhof, S., et al. Generalized bulk–boundary correspondence in non-Hermitian topolectrical circuits. *Nat. Phys.* **16,** 747–750 (2020).

35. Stegmaier, A., Imhof, S., Helbig, T., Hofmann, T., Lee, C. H., Kremer, M., ... & Thomale, R. (2021). Topological defect engineering and PT symmetry in non-Hermitian electrical circuits. Physical Review Letters, 126(21), 215302.

36. Lee, C. H., Imhof, S., Berger, C., Bayer, F., Brehm, J., Molenkamp, L. W., ... & Thomale, R. (2018). Topolectrical circuits. Communications Physics, 1(1), 39.

37. Hofmann, T., Helbig, T., Lee, C. H., Greiter, M., & Thomale, R. (2019). Chiral voltage propagation and calibration in a topolectrical Chern circuit. *Physical review letters*, *122*(24), 247702.

38. Xiao, D., Chang, M. C. & Niu, Q. Berry phase effects on electronic properties. *Rev. Mod. Phys.* **82,** 1959–2007 (2010).

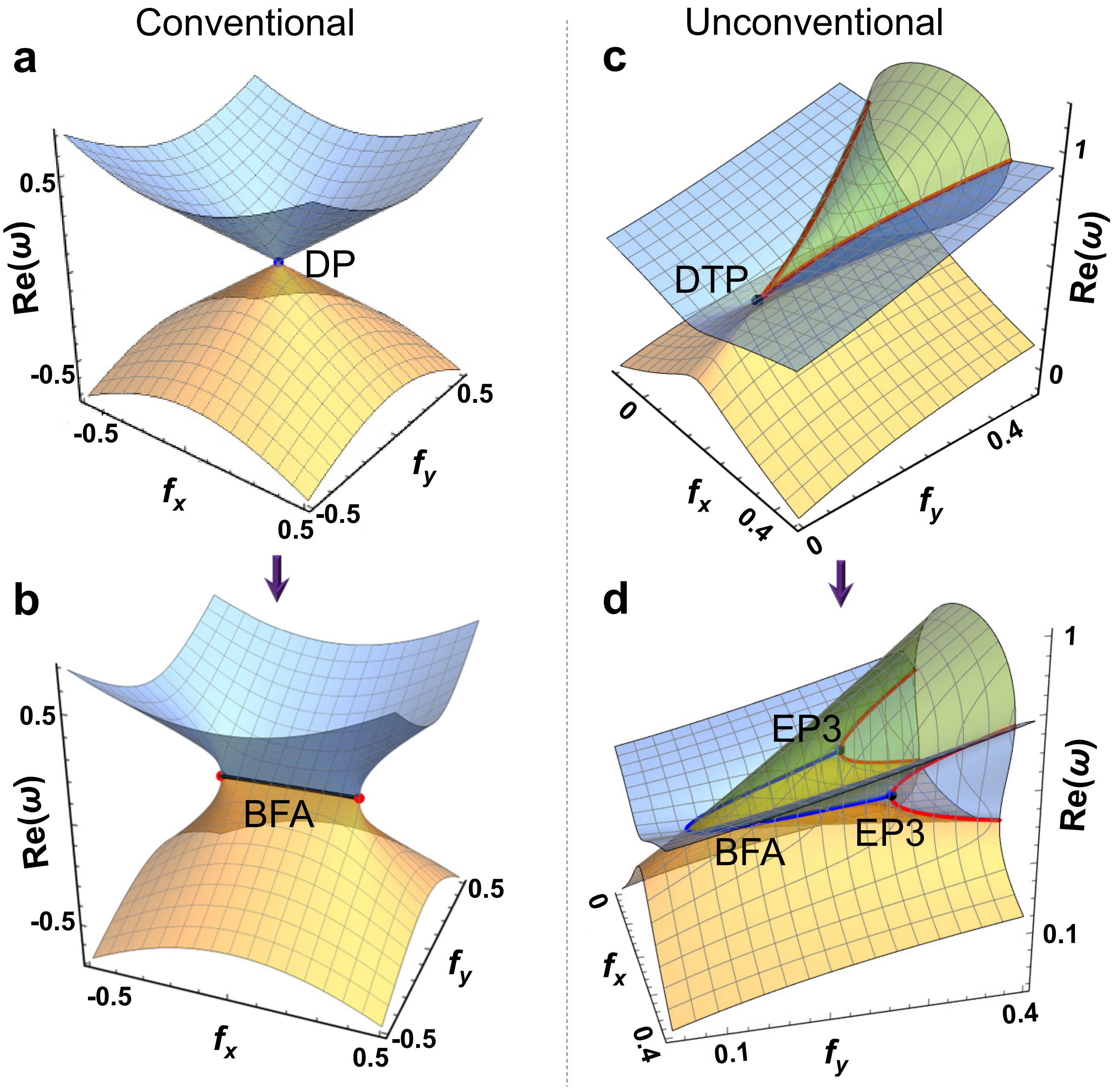
Conventional
Unconventional
a
0.5
Re(ω)
DP
-0.5
-0.5
f_x
0.5
-0.5
f_y
0.5
b
0.5
Re(ω)
BFA
-0.5
-0.5
f_x
0.5
-0.5
f_y
0.5
c
1
Re(ω)
DTP
0
0
f_x
0.4
0
f_y
0.4
d
1
Re(ω)
EP3
EP3
BFA
0
f_x
0.4
0.1
f_y
0.4
0.1

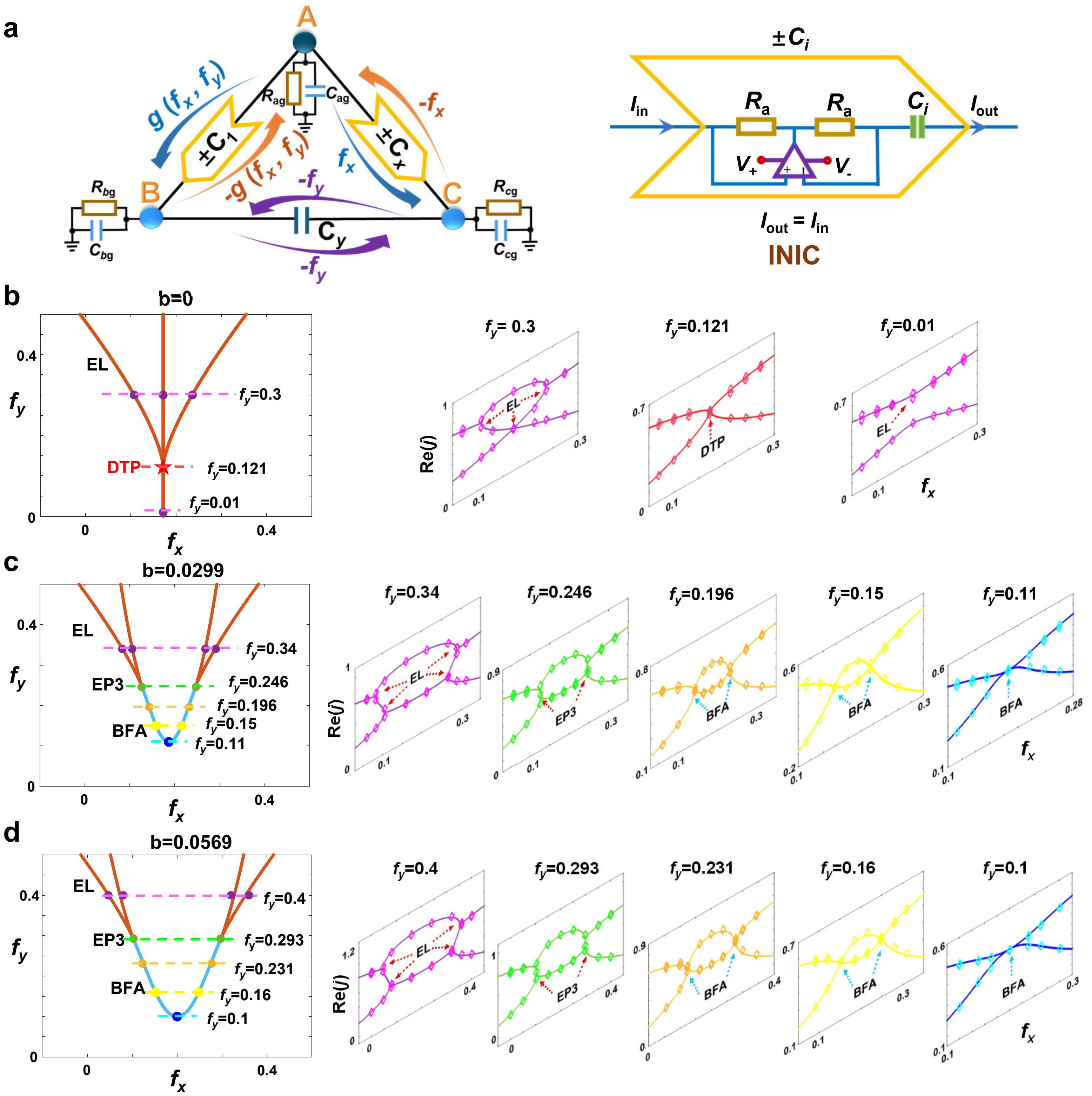
a
A
B
C
g (f_x, f_y)
R_ag
C_ag
±C_1
±C_x
-f_x
f_x
-g (f_x, f_y)
-f_y
C_y
-f_y
R_bg
C_bg
R_cg
C_cg
±C_i
I_in
R_a
R_a
C_i
I_out
V_+
V_-
I_out = I_in
INIC
b
b=0
EL
f_y=0.3
DTP
f_y=0.121
f_y=0.01
f_y
f_x
0
0.4
f_y= 0.3
f_y=0.121
f_y=0.01
Re(j)
EL
DTP
EL
f_x
1
0.7
0.7
0.1
0.3
c
b=0.0299
EL
f_y=0.34
EP3
f_y=0.246
f_y=0.196
f_y=0.15
BFA
f_y=0.11
f_y=0.34
f_y=0.246
f_y=0.196
f_y=0.15
f_y=0.11
Re(j)
EL
EP3
BFA
BFA
BFA
f_x
0.9
0.8
0.6
0.6
0.28
d
b=0.0569
EL
f_y=0.4
EP3
f_y=0.293
f_y=0.231
BFA
f_y=0.16
f_y=0.1
f_y=0.4
f_y=0.293
f_y=0.231
f_y=0.16
f_y=0.1
Re(j)
EL
EP3
BFA
BFA
BFA
f_x
1.2
0.9
0.7
0.6

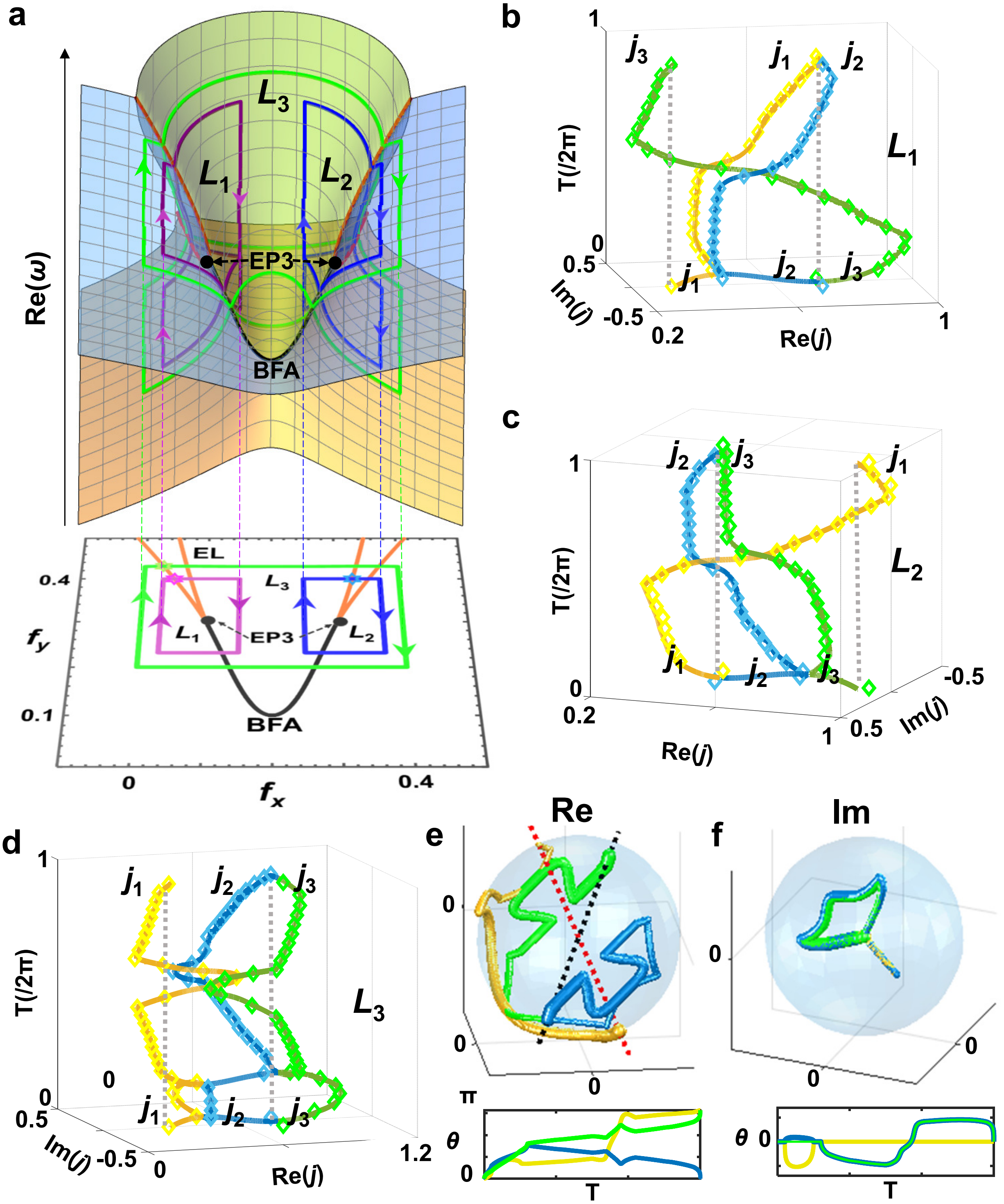
a
Re(ω)
L3
L1
L2
EP3
BFA
EL
0.4
0.1
f_y
0
0.4
f_x
b
1
0
0.5
-0.5
0.2
1
T(/2π)
Im(j)
Re(j)
j_1
j_2
j_3
L1
c
1
0
0.2
1
0.5
-0.5
T(/2π)
Re(j)
Im(j)
j_1
j_2
j_3
L2
d
1
0
0.5
-0.5
0
1.2
T(/2π)
Im(j)
Re(j)
j_1
j_2
j_3
L3
e
Re
0
0
0
π
θ
0
T
f
Im
0
0
0
θ
0
T

Supplementary Information: Unconventional bulk-Fermi-arc links paired third-order exceptional points splitting from a defective triple point

Jing Hu, Ruo-Yang Zhang, Mudi Wang, Dongyang Wang, Shaojie Ma, Jian Huang, Linjun Wang,
Xiaoping Ouyang, Yifei Zhu, Hongwei Jia*, C. T. Chan*

Supplementary Note 1: Experimental errors and impact of EP3 sensitivity

In the circuit experimental setup (Fig. S1), experimental errors are inevitable and arise from various factors, including measurement inaccuracies of the instruments, internal resistance of the circuits, as well as parasitic capacitance and resistance. In this section, we present a detailed analysis of these experimental errors. Additionally, we highlight the high sensitivity of the EP3s, which makes them particularly susceptible to such errors, and provide a discussion of their impact on the experimental results.

We begin by presenting the data on the experimental errors. Figures S2 and S3 correspond to the data in Fig. 2b-d and Fig. 3b1, b2, c1 in the main text, respectively. The deviations between the experimental and theoretical results are illustrated with error bars. The analysis shows that for most parameter values, the errors are relatively small. However, at degeneracies, such as EL, EP3, and DPT, the errors become larger. Notably, even at the BFA, which is not a degeneracy, the error is larger compared to non-degenerate parameters. The maximum errors for each type of point are summarized in Table S1. Among these, the error at EP3 is the largest. This can be attributed to the fact that EP3 represents a third-order degeneracy and exhibits high sensitivity to parameter variations and system symmetries.

In the experiments, it is challenging to precisely set the selected parameter (capacitance value) to the theoretical EP3, and maintaining exact symmetries is hindered by the parasitic capacitance and resistance of the circuit elements. To identify the most experimentally approximated EP3, measurements were taken at points near the theoretical EP3. For instance, in Fig2.b2 for f_y= 0.246, the theoretical EP3 is located at f_x=0.12702175, To approximate this, measurements were conducted at the close parameters f_x=0.126, f_x=0.1265, f_x=0.127 with the resulting admittance eigenvalues compared. The real parts of the experimental eigenvalues are indicated with green arrows in Fig. S5, which shows the experimental error is smallest and the closest approximation to the EP3 occurs at f_x=0.126. Despite the small difference of 0.0005 among the three experimental parameters, the results vary obviously due to the high sensitivity of the EP3.

Supplementary Note 2: Defining the winding number of the EP3 with resultant vector

Now we review the derivation process [3] of the form Eq. (2) in the main text using the resultant. Such a method only considers the evolution of eigenvalues in a loop but does not consider the eigenstates behavior, and hence does not capture the topological information encoded in the eigenstates [4]. However, such an approach is still useful as it explains the stability of these high order EPs [3], despite that it cannot demonstrate the topological nontriviality of paired EP3s lying on the cusps. We use this form to define the winding number of a single EP3, and EP3s with opposite windings can merge. Notably, this winding number cannot demonstrate that the EP3 pair is topologically nontrivial, as Eq. (2) provides a trivial result W=0 integrated along l_3 that encloses the EP3 pair. Similarly, by applying Eq. (2) on a closed loop enclosing the DPT, one also obtains a trivial result W=0. Paired EPs connected by the BFA together generally carry nontrivial topology [5,6], therefore, this winding number, which only considers the eigenvalues, is insufficient in visualizing the topological nontriviality of the paired EP3s.

We start from the characteristic polynomial of the Hamiltonian

$$P_f(\omega) = \det[H(f)-\omega] = a_n(f)\omega^n + a_{n-1}(f)\omega^{n-1} + \ldots + a_1(f)\omega + a_0(f) \tag{S1}$$

where H is the Hamiltonian matrix, ω is the eigenvalue, and f defines the parameter space. We here consider

2D parameter space, and therefore f has two components f_x and f_y. The set $\{a_n(f),\ldots,a_0(f)\}$ are functions of the parameter space, and for our cases, these functions are real because the system has *PT* symmetry. The integer n shows that the Hamiltonian is an $n\times n$ matrix. At a μth-fold degeneracy (ω_μ at f_μ), $P_{f_\mu}(\omega_\mu)$ must vanish. Since ω_μ is the μ-multiple root of $P_{f_\mu}(\omega)$, the successive derivatives $P^{(i)}_{f_\mu} = \partial^i P_{f_\mu}(\omega)/\partial\omega^i$ (i=1, 2, 3, …, μ–1) must also vanish at ω_μ (we note that $P^{(0)}_{f_\mu} = P_{f_\mu}$). This information is encoded into the zeros of the resultant. In mathematics, the resultant of two polynomials R_{P_1,P_2} is a polynomial expression of their coefficients that is equal to zero if and only if the polynomials have a common root [3]. The resultant is obtained as $R_{P_1,P_2} = \det[S_{P_1,P_2}]$, where S_{P_1,P_2} is the Sylvester matrix of P_1 and P_2. For example, with the polynomials $P_1=a_nx^n+a_{n-1}x^{n-1}+a_{n-2}x^{n-2}+\ldots+a_0$ and $P_2=b_mx^m+b_{m-1}x^{m-1}+b_{m-2}x^{m-2}+\ldots+b_0$, one can obtain their Sylvester matrix

$$S_{P_1,P_2} = \left[\begin{array}{cccccccc}
a_n & 0 & \cdots & 0 & b_n & 0 & \cdots & 0 \\
a_{n-1} & a_n & \cdots & 0 & b_{n-1} & b_n & \cdots & 0 \\
a_{n-2} & a_{n-1} & \ddots & 0 & b_{n-2} & b_{n-1} & \ddots & 0 \\
\vdots & \vdots & \ddots & a_n & \vdots & \vdots & \ddots & b_n \\
a_0 & a_1 & \cdots & \vdots & b_0 & b_1 & \cdots & \vdots \\
0 & a_0 & \ddots & \vdots & 0 & b_0 & \ddots & \vdots \\
\vdots & \vdots & \ddots & a_1 & \vdots & \vdots & \ddots & b_1 \\
0 & 0 & \cdots & a_0 & 0 & 0 & \ddots & b_0 \\
\multicolumn{4}{c}{\underbrace{\hphantom{a_{n-1}\quad a_{n-1}\quad \cdots\quad a_0}}_{m}} & \multicolumn{4}{c}{\underbrace{\hphantom{b_{n-1}\quad b_{n-1}\quad \cdots\quad b_0}}_{n}}
\end{array}\right] \tag{S2}$$

Since $P^{(i)}_{f_\mu}$ (i=0, 1, 2, 3, …, μ–1) all have a common root ω_μ, one can obtain a set of null resultants at f_μ

$$R_{P^{(i-1)}_{f_\mu},P^{(i)}_{f_\mu}} = 0 \quad \text{with } i=1, 2, 3, \ldots, \mu-1 \tag{S3}$$

This equation is actually a necessary and sufficient condition for obtaining a μth-fold degeneracy. Since a μth-fold degeneracy can be of different forms, for example in our considered Hamiltonians, a three-fold degeneracy can be an EP3 or a DTP. Obtaining them utilizes the same condition Eq. (S3), it is therefore unprecise to claim that Eq. (S3) is a necessary and sufficient condition for obtaining a EP3 in Ref. [3]. The set of resultants can form a vector with μ–1 components

$$R = (R_1, R_2, R_3, \ldots, R_{\mu-1}) = (R_{P_{f_\mu}^{(0)}, P_{f_\mu}^{(1)}}, R_{P_{f_\mu}^{(1)}, P_{f_\mu}^{(2)}}, R_{P_{f_\mu}^{(2)}, P_{f_\mu}^{(3)}}, \ldots, R_{P_{f_\mu}^{(\mu-2)}, P_{f_\mu}^{(\mu-1)}}) \qquad \text{(S4)}$$

It is obvious that the vector R forms a vector field in the parameter space, and is critical ($R=\mathbf{0}$) at the μth-fold degeneracy. We therefore can define a winding number for the critical point with the vector field R. Let us take EP3 lying on the cusp of EL as an example. The vector field has two components R_1 and R_2 because $\mu=3$, and only has one critical point, lying on the EP3. We note that R is not a zero vector at EL because the R_2 component is not zero at the EL, which exclude the impact of the singular ELs in defining the winding numbers. The winding number can be defined with the normal vector of R [i.e., $(-R_2, R_1)$]

$$W = \frac{1}{2\pi}\oint \frac{-R_2 dR_1 + R_1 dR_2}{|R_2^2 + R_1^2|} \qquad \text{(S5)}$$

We can insert $dR_1 = \partial R_1 / \partial f_x df_x + \partial R_1 / \partial f_y df_y$ and $dR_2 = \partial R_2 / \partial f_x df_x + \partial R_2 / \partial f_y df_y$

$$\begin{aligned} W &= \frac{1}{2\pi}\oint \frac{(R_1 \partial R_2 / \partial f_x - R_2 \partial R_1 / \partial f_x) df_x + (R_1 \partial R_2 / \partial f_y - R_2 \partial R_1 / \partial f_y) df_y}{|R_2^2 + R_1^2|} \\ &= \frac{1}{2\pi}\sum_{\alpha=x,y}\oint \frac{(R_1 \partial R_2 / \partial f_\alpha - R_2 \partial R_1 / \partial f_\alpha) df_\alpha}{|R_2^2 + R_1^2|} \end{aligned} \qquad \text{(S6)}$$

Then Eq. (2) in the main text can be obtained.

The derivation details here follow Ref. [3]. This form [i.e., Eq. (S6)] has several advantages over the Berry connection approach. The most important advantage is that this equation overcomes the ill-defined Berry connection at ELs. We know that the Berry phase integral cannot be calculated if the closed loop intersects ELs. There could also be some disadvantages, for example, the vector field R cannot distinguish different forms of degeneracies of the same fold, which is obvious from our systems as EP3 and DTP are inherently different although they are both three-fold degeneracies. They are both critical points $R=0$ of the vector field. This disadvantage comes from the fact that this method simply considers the evolution of eigenvalues (as displayed in Fig. 3b-c in the main text) but ignores the topological information encoded in the eigenstates. However, the eigenstates always encode additional topological information, which supplements Eq. (S13) which simply provides a trivial topological characterization for a loop encircling the EP3 pair or the DPT. We address this issue in the next section, as we obtain information from the eigenstates.

Supplementary Note 3: Characterizing the topology of a loop encircling hypersurface singularities with eigenframe

In this section, we will show that the eigenframe evolution as parameters vary includes both deformation and rotation processes, resulting from the inner product space of the eigenframe. Our considered systems have both *PT* symmetry (Hamiltonian H is real $H=H^*$) and an additional η-pseudo-Hermitian symmetry ($\eta H\eta^{-1}=H^\dagger$), which means that $\eta H\eta^{-1}=H^\dagger=H^T$ (the superscript T means transpose). This relation determines the evolution of the eigenframe [7,8]. We first look at the left and right eigenvalue problems

$$H^T\varphi'_m=\omega\varphi'_m,\ H\varphi_m=\omega\varphi_m \tag{S7}$$

where φ'_m and φ_m denote the left and right eigenstates respectively, corresponding to the same eigenvalue ω. The symmetries impose $\eta H\eta^{-1}\varphi'_m=\omega\varphi'_m$, meaning that

$$H\eta^{-1}\varphi'_m=\omega\eta^{-1}\varphi'_m \tag{S8}$$

This obviously indicates an important relationship between the left and the right eigenstates

$$\varphi'_m=\eta\varphi_m \tag{S9}$$

Non-Hermitian systems have a general biorthogonal relation $\varphi'^T_m\varphi_n=\delta_{mn}$ (Note that these eigenstates φ'^T_m and φ_n are associated with the same eigenvalue ω. Here we abandon the conventional biorthogonal relation established with the eigenstates that are associated with ω and ω^* [9], as the current form is more convient for establishing eigenframe deformation appoach), which shows an orthogonal relation of the right eigenstates via an indefinite inner product,

$$\varphi^T_m\eta\varphi_n=\delta_{mn} \tag{S10}$$

This relationship is the Minkowski-type orthogonal relation that has been provided in the Eq. (3) in the main text, and this relation determines that the eigenframe evolves in the form of Lorentz-like transformations. Here we note that the Minkowski metric has the property $\eta = \eta^{-1} = \eta^{T}$. We now consider the evolution of the eigenframe, which is governed by the equation

$$H\left|\varphi_m\right\rangle = i\partial_\lambda\left|\varphi_m\right\rangle \tag{S11}$$

where λ is the parameter that tracks the reference point on a path, and m denotes the index of the eigenstate (m=1, 2, 3). If the tracking point is off exceptional degenerate lines (i.e., ELs defined in the main text), the eigenstates are complete, and thus we can expand any field with the eigenstates

$$\phi_n(\xi(\lambda)) = \sum_m [U(\xi(\lambda))]^{-1}{}_n{}^m \varphi_m(\xi(\lambda)) \tag{S12}$$

where ξ denotes the parameter space with components ξ^1, ξ^2, ξ^3…. The linear combination form Eq. (S12) means that ϕ_n satisfies Eq. (S11). We therefore insert Eq. (S12) into Eq. (S11)

$$i\frac{\partial}{\partial\lambda}\phi(\xi(\lambda)) = H[U(\xi(\lambda))]^{-1}{}_n{}^m \varphi_m(\xi(\lambda)) \tag{S13}$$

From now on, the repeated index represents summed over according to the Einstein's summation rule [10]. The left-hand side is a partial derivative and can be expanded in view of Eq. (S12)

$$i\frac{\partial}{\partial\lambda}\phi(\xi(\lambda)) = i\frac{\partial[U(\xi(\lambda))]^{-1}{}_n{}^m}{\partial\lambda}\varphi_m(\xi(\lambda)) + i[U(\xi(\lambda))]^{-1}{}_n{}^m\frac{\partial\varphi_m(\xi(\lambda))}{\partial\lambda} \tag{S14}$$

One can use the instantaneous eigenvalue problem in static evolution problems

$$H(\xi(\lambda))\varphi_m(\xi(\lambda)) = \omega_m(\xi(\lambda))\varphi_m(\xi(\lambda)) \tag{S15}$$

We can apply a scalar product with the left eigenstate $\left\langle\varphi_l'\right|$ from the left side in Eq. (S13-S14), which gives

$$-i\omega_l[U(\xi(\lambda))]^{-1}{}_n{}^l = \frac{\partial[U(\xi(\lambda))]^{-1}{}_n{}^l}{\partial\lambda} + \left\langle\varphi_l'\right|\frac{\partial\left|\varphi_m(\xi(\lambda))\right\rangle}{\partial\lambda}[U(\xi(\lambda))]^{-1}{}_n{}^m \tag{S16}$$

The term with partial derivatives on the right-hand side can be expanded with the parameters

$$\frac{\partial\left|\varphi_m(\xi(\lambda))\right\rangle}{\partial\lambda} = \sum_{a=1,2,3\ldots}\frac{\partial\left|\varphi_m(\xi(\lambda))\right\rangle}{\partial\xi^a}\frac{\partial\xi^a}{\partial\lambda} \tag{S17}$$

Now we define an affine connection

$$A_a{}^n{}_m = -\langle \varphi'_n | \frac{\partial}{\partial \xi^a} | \varphi_m \rangle \tag{S18}$$

where Eq. (S10) is used. One can solve U^{-1} from Eq. (S16) as

$$U^{-1} = \mathrm{P}\exp\left[\int_0^\lambda ds \frac{\partial \xi^a}{\partial s} A_a - i\int_0^\lambda ds\,\omega(\xi(s))\right] = \mathrm{P}\exp\left(\int_{\xi(0)}^{\xi(\lambda)} A_a d\xi^a\right) \times \exp\left[-i\int_0^\lambda ds\,\omega(\xi(s))\right] \tag{S19}$$

The second term is a dynamical phase and thus can be ignored. The geometric phase is simply,

$$U^{-1} = \mathrm{P}\exp\left(\int_{\xi(0)}^{\xi(\lambda)} A_a d\xi^a\right) \tag{S20}$$

and P denotes the path ordering operator, because of the matrix form of the connection A. Therefore, A is exactly the non-Abelian parallel transport gauge of the eigenframe.

3.1 Topological meaningful path due to frame deformation

To encircle hypersurface singularities that are located entirely on ELs, the closed loop inevitably intersects ELs. Therefore, the loop is divided into several paths with terminal points locating on the ELs. Now we demonstrate that such open paths could be topological meaningful via the evolution of the eigenframe. We can take loop l_3 in the main text as an example. This loop is composed of four segments, with two segments α_1 and α_2 being in the exact phase sector (shaded region in Fig. S6a1), and the other two segments β_1 and β_2 in the broken phase sector. Here we define an important physical quantity, the local metric, whose entries are obtained by a bilinear-form indefinite inner product,

$$g_{mn} = \langle \varphi_m | \eta | \varphi_n \rangle \tag{S21}$$

Observing the exact phase domain that α resides in, it is not difficult to obtain that g has the diagonal form under proper normalizations

$$g = \begin{bmatrix} 1 & 0 & 0 \\ 0 & -1 & 0 \\ 0 & 0 & 1 \end{bmatrix} \tag{S22}$$

This metric form coincides with the orthogonality relation in Eq. (S10). Since g is a constant matrix, the partial derivative vanishes

$$\partial_{\xi^a} g_{mn} = 0 \tag{S23}$$

Substituting Eq. (S21) into Eq. (S23), one obtains

$$\left\langle \partial_{\xi^a} \varphi_m \middle| \eta \middle| \varphi_n \right\rangle + \left\langle \varphi_m \middle| \eta \middle| \partial_{\xi^a} \varphi_n \right\rangle = 0 \tag{S24}$$

Now we insert the identity operator $I = \sum_l |\varphi_l'\rangle\langle\varphi_l| = \sum_l |\varphi_l\rangle\langle\varphi_l'|$, Eq. (S24) reads,

$$\begin{aligned} &\sum_l \left\langle \partial_{\xi^a} \varphi_m \middle| |\varphi_l'\rangle \langle\varphi_l| \eta |\varphi_n\rangle + \sum_l \langle\varphi_m|\eta|\varphi_l\rangle \langle\varphi_l'| \middle| \partial_{\xi^a} \varphi_n \right\rangle \\ &= \sum_l \left\langle \partial_{\xi^a} \varphi_m \middle| |\varphi_l'\rangle g_{ln} + \sum_l g_{ml} \langle\varphi_l'| \middle| \partial_{\xi^a} \varphi_n \right\rangle = 0 \end{aligned} \tag{S25}$$

We note that

$$\left\langle \partial_{\xi^a} \varphi_m \middle| |\varphi_l'\rangle = \left(\langle\varphi_l'| \middle| \partial_{\xi^a} \varphi_m \right\rangle \right)^* \tag{S26}$$

meaning that

$$A^{*}{}_{\xi^a}{}^{l}{}_{m} g_{ln} + g_{ml} A_{\xi^a}{}^{l}{}_{n} = 0 \tag{S27}$$

Here we have established the relationship between the affine connection and the local metric. In the exact phase sector, the eigenstates can all be gauge to be real, and therefore, the affine connection is also real. Then Eq. (S27) is simplified

$$A_{\xi^a}{}^{l}{}_{m} g_{ln} + g_{ml} A_{\xi^a}{}^{l}{}_{n} = 0 \tag{S28}$$

The assembling of Eq. (S21) and Eq. (S27) allows one to obtain that the affine connection is a linear combination of the following generators

$$T_1 = \begin{bmatrix} 0 & 0 & 0 \\ 0 & 0 & 1 \\ 0 & 1 & 0 \end{bmatrix}, \quad T_2 = \begin{bmatrix} 0 & 0 & 1 \\ 0 & 0 & 0 \\ -1 & 0 & 0 \end{bmatrix}, \quad T_3 = \begin{bmatrix} 0 & 1 & 0 \\ 1 & 0 & 0 \\ 0 & 0 & 0 \end{bmatrix} \tag{S29}$$

It is obvious that the exponential

$$\exp(t_1 T_1 + t_2 T_2 + t_3 T_3) \tag{S30}$$

generates an SO(2,1) Lie group, which includes hyperbolic transformations characterized by T_1 and T_3, and a rotation characterized by T_2. The rotation characterized the geometric phase $\exp(\pi T_2)$ denotes that the first (φ_1) and the third eigenstates (φ_3) rotate a nontrivial π angle with φ_2 being the rotation axis. Such a situation cannot occur, because this geometric phase predicts the linear band cross between their corresponding eigenvalues (ω_1 and ω_3). However, since in an exact phase sector, the order of eigenvalues is well defined, and ω_1 and ω_3 are separated by ω_2, ω_1 and ω_3 cannot be degenerate without crossing ω_2. This prohibits the direct degeneracy between ω_1 and ω_3. Then we consider the geometric phase represented by the exponential

$$\exp\left(t_1 T_1\right)=\begin{bmatrix}1 & 0 & 0\\ 0 & \cosh t_1 & \sinh t_1\\ 0 & \sinh t_1 & \cosh t_1\end{bmatrix} \tag{S31}$$

This exponential form is different from $\exp(t_2T_2)$, because this exponential form has entries being hyperbolic functions. As $|t_1|$ increases, the exponential form diverges. However, despite such a non-converge situation, we can still consider the limits $|t_1|\rightarrow\infty$. If $t_1\rightarrow+\infty$, both $\cosh t_1$ and $\sinh t_1$ approaches $+\infty$, and we approximately have $\cosh t_1 \approx \sinh t_1=\rho$. The action of Eq. (S31) on the eigenframe gives

$$\left[\varphi_1,\varphi_2,\varphi_3\right]\exp(t_1T_1)=\left[\varphi_1,\rho(\varphi_2+\varphi_3),\rho(\varphi_2+\varphi_3)\right] \tag{S32}$$

This signifies that two eigenstates become parallel, meaning that the tracking point on the path approaches an EL formed by the degeneracy of the 2nd and the 3rd bands (e.g., the starting point of path α_1 in Fig. S6a1). Similarly, the exponential form

$$\exp\left(t_3 T_3\right)=\begin{bmatrix}\cosh t_3 & \sinh t_3 & 0\\ \sinh t_3 & \cosh t_3 & 0\\ 0 & 0 & 1\end{bmatrix} \tag{S33}$$

can be used to predict the EL formed by the 2nd and the 3nd bands, e.g., the ending point of α_1 in Fig. S6a1. If $t_1\rightarrow-\infty$, then $\cosh t_1$ approaches $+\infty$, and $\sinh t_1$ approaches $-\infty$. We therefore have the approximation $\cosh t_1 \approx -\sinh t_1=\rho$. The action of Eq. (S33) on eigenframe becomes

$$\left[\varphi_1,\varphi_2,\varphi_3\right]\exp(t_1T_1)=\left[\varphi_1,\rho(\varphi_2-\varphi_3),-\rho(\varphi_2-\varphi_3)\right] \tag{S34}$$

which obviously results in two anti-parallel eigenstates. This also means that the tracking point on the path approaches EL formed by the 2nd and the 3rd bands. The evolution of t_1 from +∞ to -∞ indicates a nontrivial path. We can consider the concatenation $\alpha_1\beta_1\alpha_2$ in Fig. S6a1 as an example, whose two terminal points are on ELs formed by the 2nd and the 3rd bands. As the tracking point moves along the path from one terminal point to the other, φ_2 and φ_3 evolve from parallel to antiparallel states (see Fig. S6a2), meaning that t_1 varies from +∞ to -∞. Such a process gives rise to a relative rotation angle between φ_2 and φ_3 quantized as π, because the two initially coalesced eigenstates bifurcate and rotate in opposite directions, and finally they are oriented in opposite directions. This is typically the eigenframe deformation process. Since this quantized relative angle emerge for an open path, the topological meaningfulness of this open path is signified. Such a situation is quite different from isolated singularities, for which an open path is generally meaningless.

In a broken phase sector, the evolution process will be more complicated and cannot be visualized with the analytical approach. However, such a frame deformation process can be extended to an open path in the broken phase sector (e.g., β_1 and β_2 in Fig. S6a1-S6b1). On such loops, there exists a similar process, because two coalesced eigenstates bifurcate to form a conjugate pair. If we track a point along a path in broken phase sector (terminal points are on ELs), the conjugate eigenstates evolve from real states to real states, the conjugate nature impose that the initial states are parallel states, and the final states are also parallel states. This means that the complex eigenstates also have a quantized relative rotation angle as 0 or 2π. This situation applies to β_1 and β_2 in Fig. S6a1-S3b1, as indicated by right panels of Fig. S6a2-S3b2, where the imaginary parts of φ_2 and φ_3 evolve from 0 to 0. It is also possible that the conjugate eigenstates evolve from real states to imaginary states, then the conjugation relation impose the final states to be antiparallel states. This loop includes a quantized relative rotation of π. However, such a situation was not applicable to these considered paths (e.g., β_1 and β_2) in this paper.

From these discussions, we can conclude that in investigating a closed loop, the eigenframe evolution process along each open path should be investigated. The overall topological characterization of the loop combines the evolution processes of all paths at the terminal points on ELs. Therefore, the topology of a hypersurface singularity not only involves the overall quantization behavior of each eigenstate along the whole loop, but also involves the quantization behavior of relative rotations along each path. Such a physical meaningful approach is compatible with intersection homotopy [11,12].

3.2 Topological equivalence relation between the paired EP3s and the DTP

In the main text, we have shown that introducing the perturbations with preserved symmetries, the DTP can be split into the EP3 pair, which comes from the topological equivalence relation between the paired EP3s and the DTP. Here we will demonstrate this equivalence with the evolution of eigenframe. A closed loop encircling the DTP is shown in Fig. S7a, and the corresponding evolution of eigenvalues along the loop is shown in Fig. S7b. As we have introduced in the main text, the BFA is the intersection of two Riemannian sheets formed by the dispersion of the real parts of eigenvalues. One is the common sheet of Re(j_2) and Re(j_3), as they are conjugate to each other j_2=j_3^* and share the same real part. The other is formed by the real eigenvalue j_1. Therefore, the BFA in our case must reside in the broken phase sector, so that only the real parts of the three eigenvalues on BFA coalesce (Note that if BFA is in exact phase regions, the BFA will be a three-fold degeneracy). The fact that the BFA is the intersection of Riemannian sheets determines that if a tracking point moves across the BFA, there has to be an order exchange of eigenvalues. This phenomenon is obvious for loops l_1 and l_2 (Fig. 3b1 and Fig. 3b2), as l_1 and l_2, which only enclose a single EL3, inevitably intersect BFA. Notably, the order exchange of eigenvalues is a swapping process of a conjugate band with the other real band (see Fig. 3b1 and Fig. 3b2), which is determined by the real parts of eigenvalues. In this context, it is obvious that the eigenvalues also do not experience order exchange along loop in Fig. S7a that encloses the DTP, similar to the situation along loop l_3 in the main text (Fig. 3c1). The eigenframe deformation and rotation process is shown in Fig. S7c, with the left and right panels showing the real and imaginary parts of the eigenstates. Through the comparison against Fig. 3c2-3c3 in the main text, we see that the evolution processes are almost identical except for some deviations in the intermediate process. Along both loops, the eigenstates φ_1 and φ_3 all evolve to their antipodal points, meaning that the accumulated angles are quantized as π (lower panels of Fig. S7c). While φ_2 evolves to the initial states without changing the sign. Such an identical processes demonstrate that the paired EP3s is topologically equivalent to the DTP, and they can both be topologically characterized as nontrivial due to the π quantization. Therefore, introducing perturbations that splits the DTP to the paired EP3s is a topologically protected process from a frame rotation perspective. This result also shows that the EP3 pair linked by the BFA in our case is topologically nontrivial. This situation is similar to the conventional case that the EP2 pair linked by a conventional BFA is topologically nontrivial [5,6]. In section 4, we will show that this topological nontriviality ensures that the DTP cannot be fully illuminated. Except for the case that the DTP can be split into paired EP3s by making b to be positive, the DTP can be split into an intersection of ELs and an isolated Dirac point by decreasing b to be negative.

3.3 Why the topological characterization approach addresses the ELs intersected by the loops

In conventional homotopic theories, the homotopic loop always avoids intersecting any degeneracy. However, if a singularity is not isolated and locates entirely on ELs, a loop encircling it will inevitably intersect the ELs. Such a loop is an intersection homotopic loop [12], which represents a new topological characterization approach distinguished from the conventional homotopy characterization. The notion of eigenframe deformation and rotation approach used here is thus a physical meaningful method that is compatible with the intersection homotopy. The key advantage of this approach is that the topological characterization result is immune to the sequence of the two conjugate bands in the broken phase sector. As a tracking point moves along a loop and crosses an EL, two eigenvalues coalesce their real parts and disparate their imaginary parts. Therefore, uncertainty of the sequence of eigenvalues is introduced by the EL degeneracy, because the upper band and lower band cannot be distinguished. However, our approach is immune to this uncertainty. We can take the loop in Fig. 4a as an example, where we have exchanged the order of j_2 and j_3 in the broken phase sector (see the comparison between Fig. 5a and Fig. 4b). In Fig. 5b, we plot the evolution process of the eigenframe. Compared with Fig. S7c, we find that the evolution of the real parts of the eigenstates remains intact, only the imaginary parts become their negatives (right panels in Fig. S8b and S7c). As we have known, the imaginary parts only serve as an intermediate process, because the eigenstates are real at the initial and the final points. That is why our approach well addresses the uncertainty caused by the EL.

Supplementary Note 4: Splitting of DTP into an intersection of ELs and a Dirac point

Although the DTP is an accidental degeneracy and is unstable, it carries nontrivial topological information. Therefore, as long as the symmetries are preserved, the DTP cannot be fully eliminated, but will be split into other forms of degeneracies. In the main text, we have shown that the DTP can be split into a pair of EP3s linked by a BFA by increasing the perturbation term b from 0 to positive. In this section, we will show that by decreasing b to negative, the DTP also becomes unstable and will be split into another two forms of degeneracies.

The results are shown in Fig. S9, where panels a and b correspond to b=-0.0299 and b=-0.0599 in Eq. (1), respectively. Here IP stands for intersection point, at which the ELs intersect transversely. While DP stands for Dirac point, which is isolated from ELs. Their corresponding dispersion diagrams (with both real and imaginary parts of eigenvalues) are shown in panels a1-a4 and b1-b4 respectively. Both IP and DP are linear band crossings as indicated by a2, a4 and b2, b4. Additionally, IP and DP are stably degeneracies, and decreasing the perturbation term *b* only makes the distance between IP and DP larger, as displayed in panels a and b.

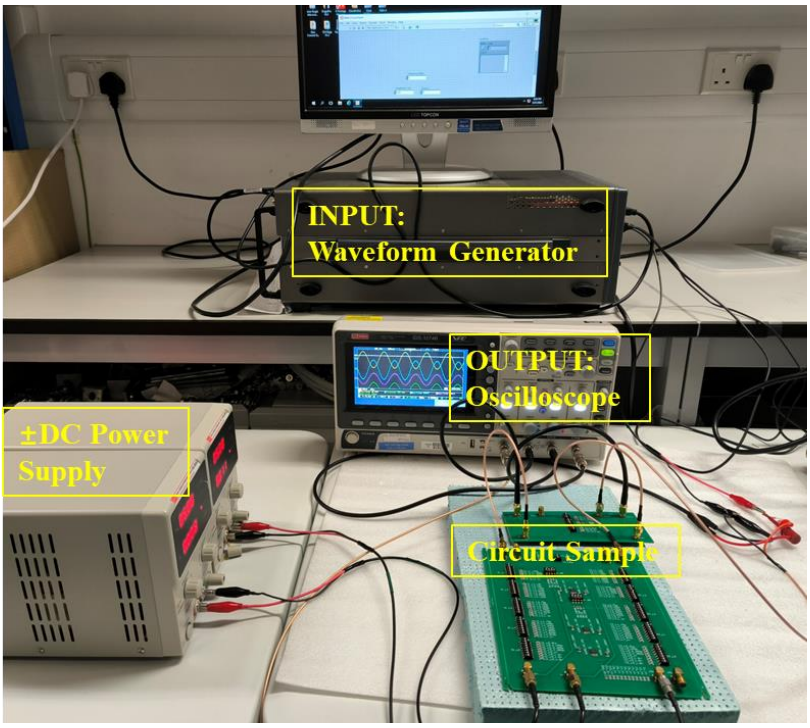

Fig. S1| Experimental setup for measuring the unconventional bulk-Fermi-arc. The instruments include the DC power supply (used for the power supply of operational amplifier), Oscilloscope (measuring output signals), and waveform generator (generating input current).

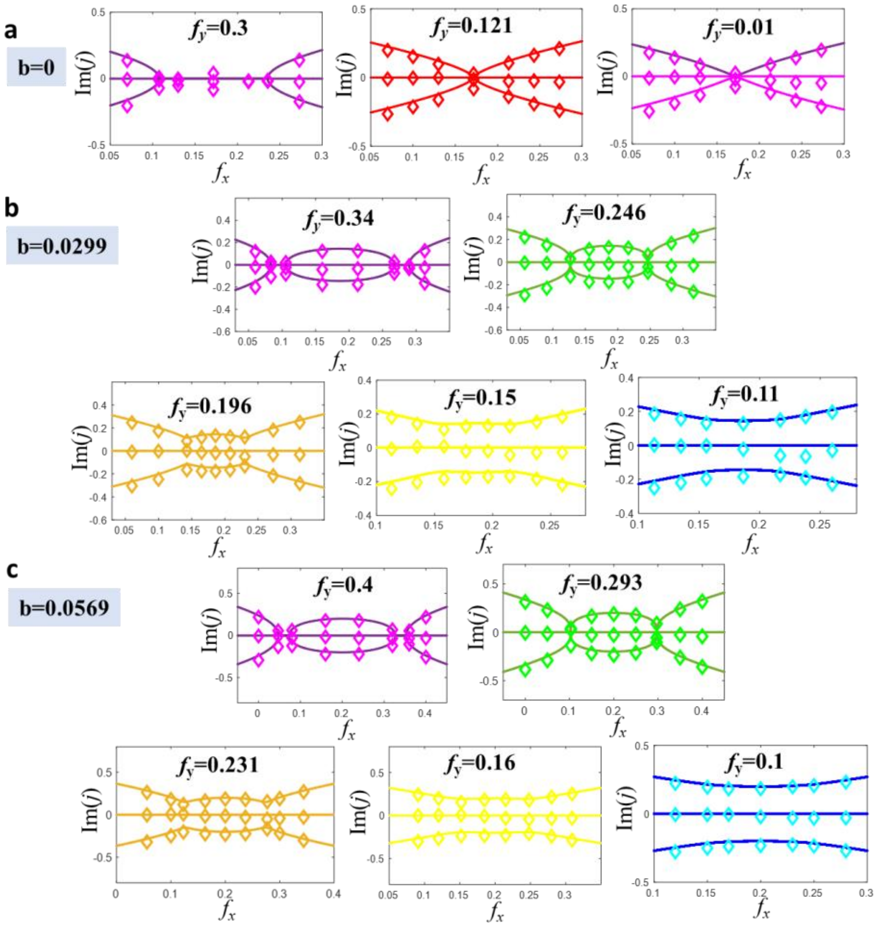

Fig. S2| Experimental and theoretical results of the dispersion of imaginary parts of the bulk-Fermi-arc. a-c are for different perturbation term *b*=0, 0.0299 and 0.0569, corresponding to b-d in the main text.

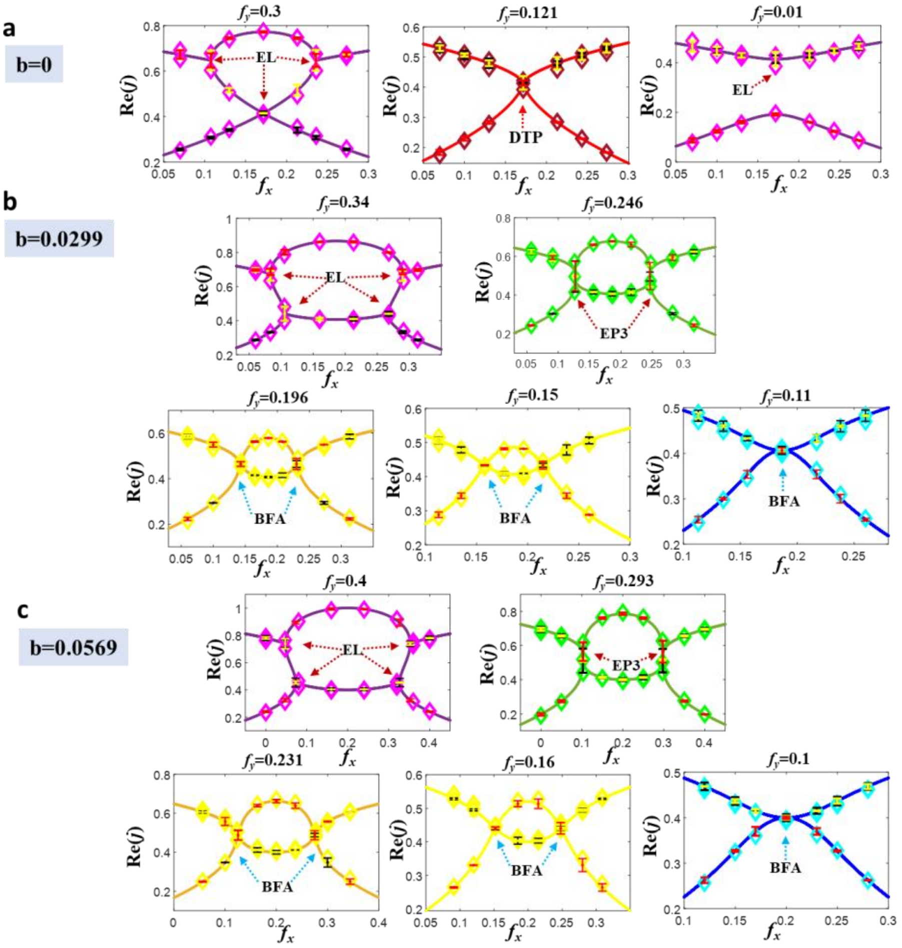

Fig. S3| Vertical error bars illustrate the experimental deviations from the theoretical results associated with the measured data in Fig. 2b-d. For each experimental data point, the middle of the error bar represents the theoretical value (indicated by the line), while the half-length of the error bar corresponds to the absolute difference between the measured eigenvalue in Fig. 2b-d and the theoretical value.

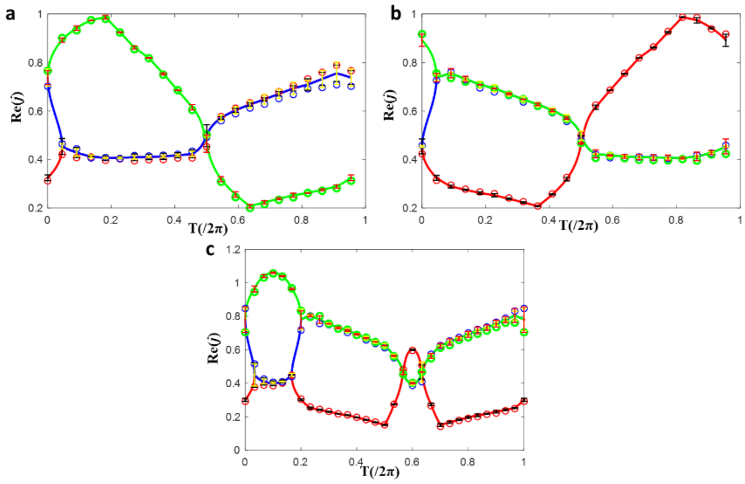

Fig. S4| Similar to Fig. S3, but panels a-c correspond to the results in Fig. 3b1, b2 and c1 in the main text, respectively.

Experimental points	**General Point**	**EL**	**DTP**	**BFA**	**EP3**
Maximum error	5%	8%	6%	6%	19%

Table S1| Maximum error in experimental measurements for each type of points.

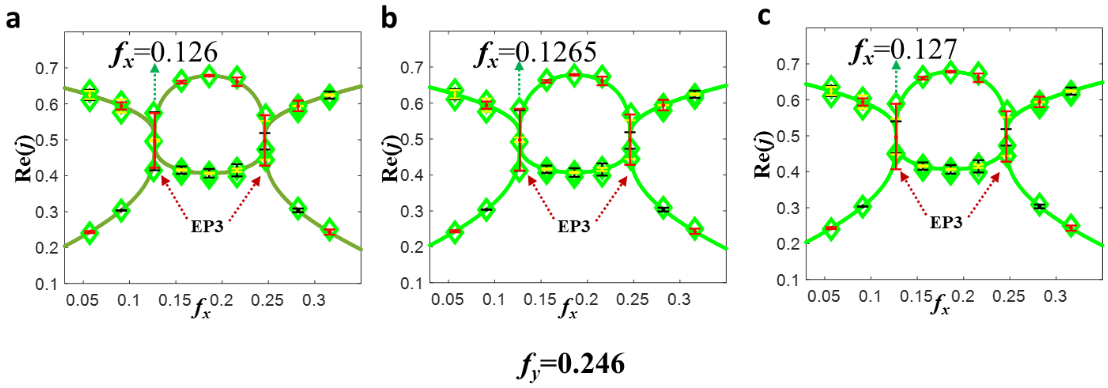

Fig. S5| The real parts of the experimental eigenvalues at the points near the theoretical EP3 for identification of the most experimentally approximated EP3.

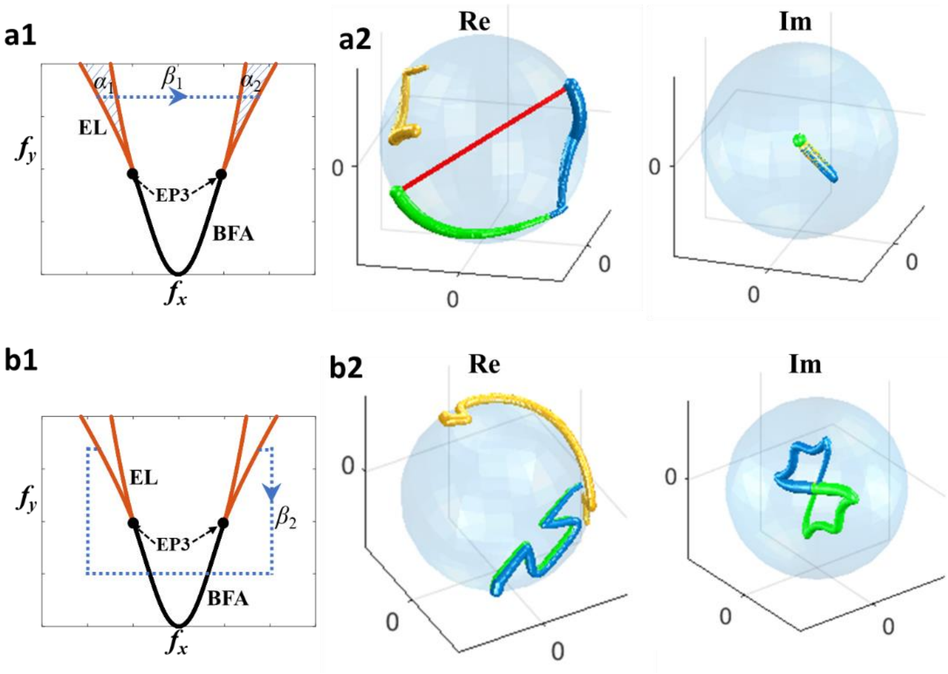

Fig. S6| Illustration of topological meaningful path. The loop l_3 in the main text can be decomposed into two parts in panels a1 (concatenation of α_1, β_1 and α_2) and b1 (path β_2), respectively. The part in panel a1 can be decomposed into three segments α_1, β_1 and α_2. All the paths are terminated at ELs. a2-b2 Eigenframe evolution processes along the concatenated path $\alpha_1\beta_1\alpha_2$ (in panel a1) and path β_2 (in panel b1).

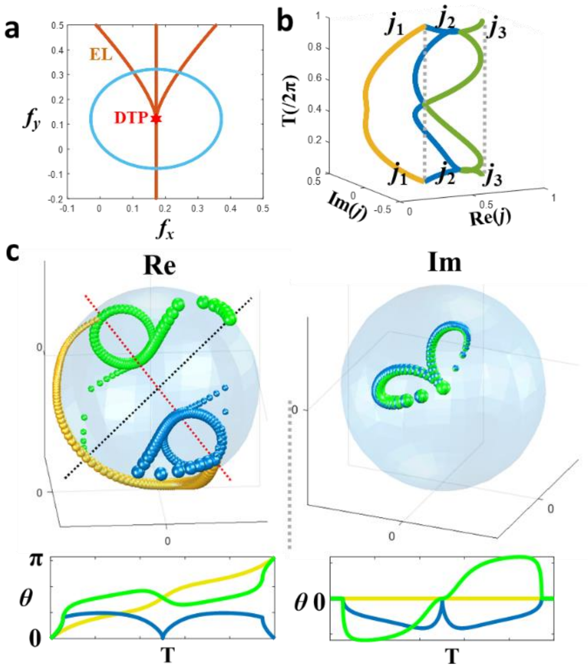

Fig. S7| Topological characterization of the DPT. a. A closed loop encircling the DTP. The DTP is adjacent to four ELs, and the loop intersects the ELs four times. b. Evolution of eigenvalues along the loop in panel a. The eigenvalues do not experience order exchange along the loop as indicated by the dashed lines. c. Evolution of eigenframe along the loop in panel a, with the left and right columns showing the real and imaginary parts of eigenstates, respectively. The eigenstates φ_1 and φ_3 evolve to their antipodal points along the loop, showing that their accumulated angles are quantized as π, as indicated by the lower panels (left). This demonstrates that the DPT is topological equivalent to the EP3 pair, because the evolution is identical to Fig. 3c2-3c3 in the main text. The evolution of the imaginary parts serves as intermediate process as the initial and final states are all real (right column of panel c).

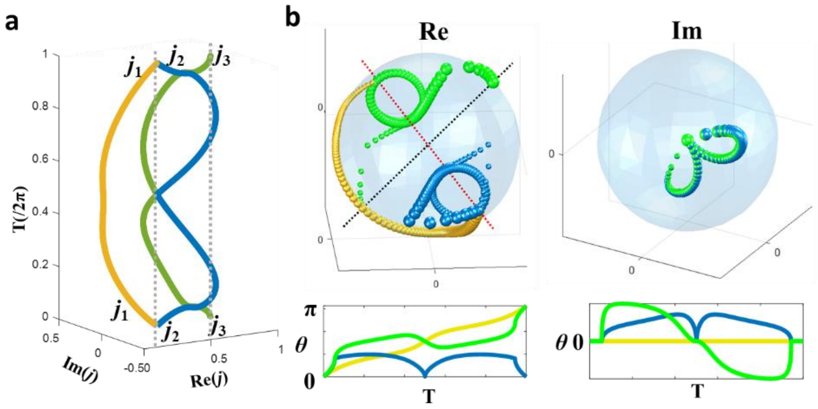

Fig. S8| Exchanging the sequence of j_2 and j_3 in the broken phase sector does not impact the topological characterization. a. Evolution of eigenvalues along the loop in Fig. S7a. The orders of j_2 and j_3 have been exchanged compared with Fig. S7b. b. Evolution of the eigenframe under the new sequence. The evolution of real parts is identical to the evolution process under the original sequence (left panel, compared with the left panel in Fig. S7c). The imaginary parts are added with a minus sign, which is only an intermediate process and does not impact the topological characterization (right panel, compared with the right panel in Fig. S7c).

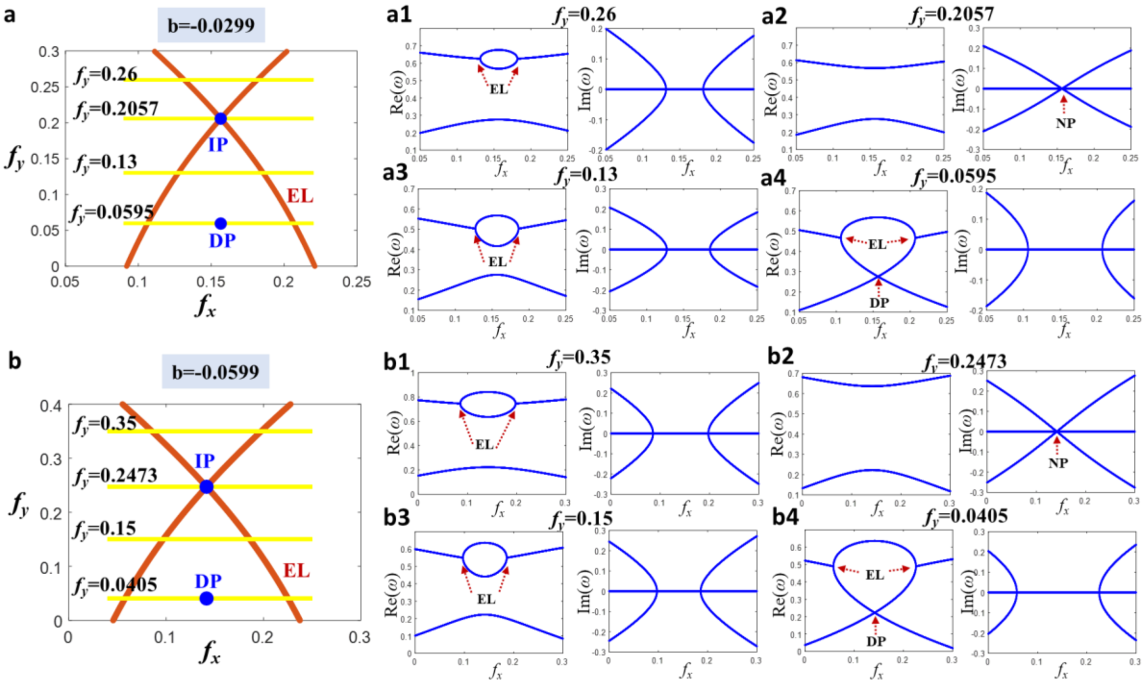

Fig. S9| a and b, degeneracies in the synthetic 2D parameter space corresponding to b=-0.0299 and b=-0.0599, respectively. a1-a4 and b1-b4, Their corresponding dispersion diagrams with both real and imaginary parts of eigenvalues on different yellow lines in panels a and b.

Supplementary References:

1. Imhof, S., Berger, C., Bayer, F., et al. Topolectrical-circuit realization of topological corner modes. *Nat. Phys.* **14,** 925–929 (2018).
2. Helbig, T., Hofmann, T., Imhof, S., et al. Generalized bulk–boundary correspondence in non-Hermitian topolectrical circuits. *Nat. Phys.* **16,** 747–750 (2020).
3. Delplace, P., Yoshida, T. & Hatsugai, Y. Symmetry-protected multifold exceptional points and their topological characterization. *Phys. Rev. Lett.* **127,** 186602 (2021).
4. Xiao, D., Chang, M. C. & Niu, Q. Berry phase effects on electronic properties. *Rev. Mod. Phys.* **82,** 1959–2007 (2010).
5. Kawabata, K., Bessho, T. & Sato, M. Classification of exceptional points and non-Hermitian topological semimetals. *Phys. Rev. Lett.* **123,** 066405 (2019).
6. Zhou, H., Peng, C., Yoon, Y., et al. Observation of bulk Fermi arc and polarization half charge from paired exceptional points. *Science* **359,** 1009–1012 (2018).
7. Jia, H., Zhang, R. Y., Hu, J., et al. Topological classification for intersection singularities of exceptional surfaces in pseudo-Hermitian systems. *Commun. Phys.* **6,** 293 (2023).
8. Hu, J., Zhang, R. Y., Wang, Y., et al. Non-Hermitian swallowtail catastrophe revealing transitions among diverse topological singularities. *Nat. Phys.* **19,** 1098–1103 (2023).
9. Kawabata, K., Shiozaki, K., Ueda, M., et al. Symmetry and topology in non-Hermitian physics. *Phys. Rev. X* **9,** 041015 (2019).
10. Freedman, D. Z. & Van Proeyen, A. *Supergravity* (Cambridge University Press, 2012).
11. Kirwan, F. & Woolf, J. *An introduction to intersection homology theory* (CRC Press, 2006).
12. Gajer, P. *The intersection Dold-Thom theorem* (State University of New York at Stony Brook, 1993).